České vysoké učení technické v Praze
Fakulta jaderná a fyzikálně inženýrská

Katedra inženýrství pevných látek
Obor: Inženýrství pevných látek

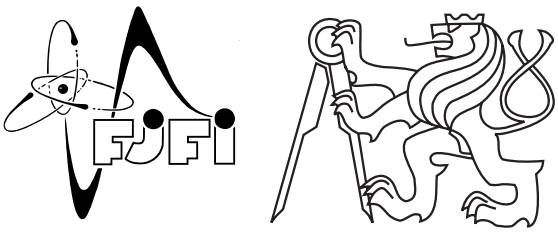

Vývoj meziatomárních potenciálů pro molekulární dynamiku pomocí neuronových sítí: Aplikace pro martensitickou fázi slitiny nikl titan

Development of neural network interatomic potentials for molecular dynamics: Application for martensitic nickel titanium

Diplomová práce

Vypracoval: Bc. Petr Jaroš
Vedoucí práce: Ing. Petr Sedlák, Ph.D.
Rok: 2024

Prohlášení

Prohlašuji, že jsem diplomovou práci vypracoval samostatně a použil jsem pouze podklady (literaturu, projekty, SW atd.) uvedené v přiloženém seznamu.

V Praze dne .....

.....

Bc. Petr Jaroš

Poděkování

Tato práce byla podpořena grantem Studenstké grantové soutěže ČVUT č. SGS22/183/OHK4/3T/14

Tato práce byla podpořena Ministerstvem školství, mládeže a tělovýchovy České republiky prostřednictvím e-INFRA CZ (ID:90254)

This work was supported by the Grant Agency of the Czech Technical University in Prague, grant No. SGS13/219/OHK4/3T/14

This work was supported by the Ministry of Education, Youth and Sports of the Czech Republic through the e-INFRA CZ (ID:90254).

Bc. Petr Jaroš

ČESKÉ VYSOKÉ UČENÍ TECHNICKÉ V PRAZE
FAKULTA JADERNÁ A FYZIKÁLNĚ INŽENÝRSKÁ
Katedra inženýrství pevných látek

ZADÁNÍ DIPLOMOVÉ PRÁCE

Student: **Bc. Petr Jaroš**

Studijní program: **Aplikace přírodních věd**

Obor: **Inženýrství pevných látek**

Akademický rok: **2022/2023**

Název práce: **Simulace mechanismů plastické deformace ve slitinách s tvarovou pamětí pomocí molekulární dynamiky.**
(česky)

Název práce: **Simulation of mechanisms of plastic deformation in shape memory alloys by molecular dynamics**
(anglicky)

Pokyny pro vypracování:
Diplomová práce bude zaměřena na simulace vývoje mikrostruktury v B19´martenzitu slitiny s tvarovou pamětí NiTi. V této slitině je unikátní kombinace silně anizotropní plastické deformace zprostředkované pouze jedním skluzovým systémem s vysoce pohyblivými hranicemi typu dvojčat. Předpokládá se, že spřažením těchto dvou mechanismů vzniká nový, jedinečný mechanismus plastické deformace, jež stojí ze neobvykle velkou houževnatostí této slitiny. Simulace interakce plastického skluzu s pohyblivou dvojčatovou hranicí bude provedena pomocí molekulární dynamiky. Diplomová práce se zaměří především na sestavení vhodného atomárního potenciálu pro tento systém. S ohledem na složitost simulovaného materiálu se dá předpokládat, že běžně používané parametrizace atomárních potenciálů (EAM, MEAM) budou příliš restriktivní. Diplomant se tak zaměří na využití moderního, obecnějšího vyjádření potenciálu s použitím neurálních sítí (NN).

Při řešení postupujte podle následujících bodů.

1) Proveďte rešerši základních NN atomárních potenciálů využívaných k simulaci pevných látek.
2) Pro vzorový případ – monokrystal Si, navrhněte NN potenciál. Jako referenční dataset použijte jednak struktury s energiemi určenými DFT výpočtem, jednak struktury s energiemi z existujících MEAM potenciálů pro Si.
3) Ověřte vhodnost NN potenciálu vzhledem k základním vlastnostem Si (strukturní parametry, elastické konstanty, fononové spektrum, Grüneisenovy parametry), diskutujte vztah NN a MEAM potenciálů.
4) Uveďte přehled základních vlastností slitiny NiTi s tvarovou pamětí, zaměřte se především na mechanismy plastické deformace a vliv plastické deformace na funkční chování slitiny.

5) Navrhněte NN potenciál pro binární slitinu NiTi. Za výchozí referenční dataset použijte struktury s energiemi z existujících MEAM potenciálů a DFT výpočtů. Ověřte vhodnost potenciálu vzhledem k základním vlastnostem slitiny NiTi a k možnosti simulovat anizotropní plastický skluz a pohyb hranic typu dvojčat.

Doporučená literatura:

[1] Behler, J. (2021). Four generations of high-dimensional neural network potentials. Chemical Reviews, 121(16), 10037-10072.

[2] Tuckerman, M. E. Statistical Mechanics : Theory and Molecular Simulation, isbn: 9780191523465. https://ebookcentral.proquest.com (Oxford: Oxford University Press, 2010).

[3] Plimpton, S., Thomson, A., Crozier, P., Kohlmeyer, A. (2022) LAMMPS Massive-Parallel Atomistic Simulator Manual

[4] Šittner, P., Sedlák, P., Seiner, H. , et al.. (2018). On the coupling between martensitic transformation and plasticity in NiTi: Experiments and continuum based modelling. Progress in Materials Science, 98, 249-298.

Jméno a pracoviště vedoucího práce:
Ing. Petr Sedlák, Ph.D.., Katedra inženýrství pevných látek, FJFI ČVUT.

Jméno a pracoviště konzultanta:
Ing. Javier Varillas Delgado, Ph.D., Ústav termomechaniky, AVČR.

Datum zadání diplomové práce: 20. 10. 2022

Termín odevzdání diplomové práce: 7. 5. 2023

Doba platnosti zadání je dva roky od data zadání.

……
garant

…… ……..
vedoucí katedry *děkan*

V Praze dne 20. 10. 2022

Název práce:

Vývoj meziatomárních potenciálů pro molekulární dynamiku pomocí neuronových sítí: Aplikace pro martensitickou fázi slitiny nikl titan

Autor: Bc. Petr Jaroš

Obor: Inženýrství pevných látek

Druh práce: Diplomová práce

Vedoucí práce: Ing. Petr Sedlák, Ph.D.
Katedra inženýrství pevných látek
Fakulta jaderná a fyzikálně inženýrská
České vysoké učení technické v Praze

Konzultant: Ing. Javier Varillas Delgado, Ph.D.
Ústav termomechaniky, AVČR

Abstrakt: Tato práce se zaměří na studium mechanismů plastické deformace a vývoje mikrostruktury martenzitických krystalů NiTi B19' pomocí atomistických simulací. NiTi vykazuje jedinečnou kombinaci silně anizotropní plastické deformace zprostředkované pouze jedním systémem skluzu s vysoce pohyblivými hranicemi typu dvojčat, přičemž se předpokládá, že spojení těchto dvou mechanismů vytváří jedinečný plastický proces, který způsobuje houževnatost B19' NiTi. Vzhledem ke složitosti martenzitické fáze B19' mají dosavadní potenciály (např. 2NN-MEAM) problém podchytit všechny vlastnosti ovlivňující plastickou deformaci . Tato práce se zaměří na vývoj nového meziatomárího potenciálu pomocí metod neuronových sítí, který by překonal dosavadní analytické meziatomární potenciály.

Klíčová slova: Molekulární dynamika, meziatomární potenciály, neuronové sítě, NiTi, slitiny s tvarovou pamětí

Title:

Development of neural network interatomic potentials for molecular dynamics: Application for martensitic nickel titanium

Author: Bc. Petr Jaroš

Abstract: This thesis focuses on the study of the plastic deformation mechanisms and microstructure evolution of B19' martensitic NiTi crystals through atomistic simulations. This phase exhibits a unique combination of strongly anisotropic plastic deformation mediated by only one slip system with highly mobile twin-type boundaries, where the coupling of these two mechanisms is believed to create a unique plastic process that governs the high toughness of B19' NiTi. The computational analysis of the plastic slip pathways is carried out by molecular dynamics. Considering the complexity of the plastic phenomena occurring in B19' martensitic crystals, the parametrizations of available interatomic potentials for Ni-Ti systems (such as the 2NN-MEAM model) are deemed to be insufficient for an accurate prediction of these complex plastic processes. Based on that, the student develops potential for NiTi using neural networks, evaluating their accuracy by way of comparison to the theory and experiments.

Key words: Molecular dynamics, interatomic potential, neural networks, NiTi, shape memory alloys

Contents

Introduction

Atom-level analysis can provide insightful information about the processes occurring in material systems, thus helping to understand the governing mechanisms that determine the physical properties of materials. Molecular dynamics simulations, a computational tool, play an important role in understanding the dynamic behavior of materials. The accuracy of these simulations is heavily dependent on the interatomic potentials used to describe the interactions between atoms within a system. Traditional analytical potentials, such as the Tersoff or 2NN-MEAM potential, have long been employed for metallic systems because of their computational efficiency, but their ability to predict complex interactions is limited.

In recent years, there has been introduced an entirely new approach, which serves to develop high-accuracy interatomic potential: the neural network (NN) potentials. This approach uses machine learning techniques, to develop interatomic potentials that overcome the limitations of traditional analytical models and essentially bring the precision of density functional theory into molecular dynamics.

The main focus of this work is to develop NN potential for the B19' martensitic phase of NiTi. While many existing potentials are focused on the simulation of the transformation between the B2 austenitic and B19' martensitic phases, the NN potential aims to describe the plastic deformation in the martensitic B19' phase of NiTi. It was newly suggested in Ref. [1], that the plastic deformation in the martensitic phase can play an important role in the reversibility of phase transformation in NiTi. The confirmation of such a claim demands extensive study on the atomistic level.

As a proof of concept, I develop the NN potential for silicon. I will compare the result of the NN potential of silicon with the existing Tersoff potential. The comparison involves a study of basic elastic and dynamical properties such as the elastic constant and phonon dispersion curves. Finally, I will build the NN potential for NiTi and compare the basic mechanical properties predicted by this potential with the analytical 2NN-MEAM potential. In this regard, attention is directed to the behavior of the B19' martensitic phase under shearing on the (100) slip plane.

Theoretical background

1.1 Molecular dynamics

Molecular dynamics (MD) is a computational approach that simulates the time evolution of a system composed of atoms, which are defined by their position $\mathbf{r}$, and velocity $\mathbf{v}$. This technique can simulate systems containing hundreds of thousands of atoms on the time scale of nanoseconds. The computation of the time evolution is done by iteratively solving Newton's equation of motion, where the acting forces are determined by interatomic potential. The statistical properties such as temperature, pressure, and volume are controlled by the statistical ensemble [2]. A simplified workflow of the MD is shown in Figure 1.1

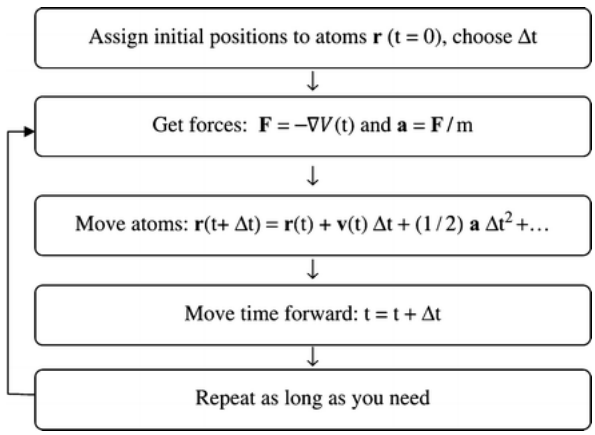

Figure 1.1: A simplified workflow of an MD. Figure taken from Ref. [3].

The Verlet algorithm is a common numerical approach that calculates the discrete evolution of the system from t to $t+\Delta t$. This algorithm is based on Taylor's expansion of the time-dependent position $\mathbf{r}(t)$

$$\boldsymbol{r_i}(t+\Delta t) \approx \boldsymbol{r_i}(t) + \frac{d\boldsymbol{r}_i(t)}{dt}\Delta t + \frac{1}{2}\frac{d^2\boldsymbol{r}_i(t)}{d^2t}(\Delta t)^2 = \boldsymbol{r_i}(t) + \boldsymbol{v_i}(t)\Delta t + \frac{\boldsymbol{a_i}(t)}{2}(\Delta t)^2 \quad (1.1)$$

by the application of Taylor's expansion for step $+\Delta t$ and $-\Delta t$ and summing up these two expansions, the Verlet algorithm is obtained

$$\boldsymbol{r_i}(t+\Delta t) = 2\boldsymbol{r_i}(t) - \boldsymbol{r_i}(t-\Delta t) + \frac{1}{m_i}\boldsymbol{F}_i(t)(\Delta t)^2 \quad (1.2)$$

In this work, I will focus on the determination of acting forces through the interatomic potentials. A more detailed description of the MD technique can be found in my bachelor thesis [3], or in Ref. [4].

1.2 Neural networks

Thanks to the increasing computing power, the calculation of highly complex tasks becomes possible. However, tasks that seem easy to humans can be problematic for computers, for example recognizing an image, a font or a digit can be difficult. To solve this problem, so-called machine learning methods started to be used. Machine learning is a very brought term, but in general refers to mathematical and statistical methods, that help algorithms find solutions without knowing at the beginning. Finding the solution is done using learning, which can be defined as [4]:

A computer program is said to learn from experience E concerning some class of tasks T and performance measure P, if its performance at tasks in T, as measured by P, improves with experience E.

It is clear from the definition that three parts are needed to go through the process of learning. A computer program (model) e.g. neural network and a task, in my case the task is to predict the energy. A source of experience, for me, it is a data set of structures with corresponding energies. Finally, we need some reference to whether the prediction of the model has improved or not.

1.2.1 Basics of neural networks

One of the most used machine learning approaches is called neural networks. This method is inspired by neural synapses in the brain. A typical neural network model consists of many interconnected layers, each layer contains many mathematical functions called neurons, and the number of neurons determines the size of the layer. A feed forward neural network, which will be used in this work, is usually divided into three parts. The first part is called the input layer, which is only one layer containing input data. The second part consists of several hidden layers, size can vary depending on the size of the data set and the purpose of the neural network. The last part is called the output layer and represents the prediction of the neural network. This classification is schematically shown in Figure 1.2.

All neurons in the layer are connected to the neighboring layers by weights, which represent the importance of the neuron's connection and each neuron has its own bias, which can be understood as a threshold for accepting the value of the neuron [5]. This is described in

$$y \equiv f(wx + b) \tag{1.3}$$

where w refers to the weight, b refers to bias, x denotes the input value for the neuron and y represents the output value of the neuron. In equation (1.3), $f(...)$ is the activation function, which has a fundamental role. Activation functions are usually

non-linear and smooth. Non-linearity ensures that neural networks are capable of capturing more complex problems. A neural network with a linear function is essentially just a linear regression model. The smoothness of the activation function ensures differentiability, thus the possibility to transfer an effect of small changes in weights or biases to the final prediction. Activation functions can take many forms and can improve the predicting abilities of neural networks.

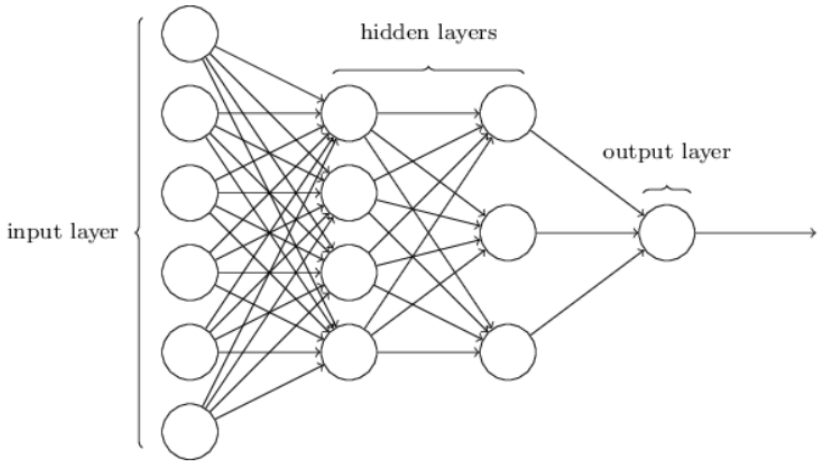

Figure 1.2: A general architecture of a neural network containing the input layer, hidden layers, and the output layer. The figure is taken from Ref. [5].

In general, let w_{ij}^{kl} be the weight between neuron i in layer k and neuron j in layer l, where $l = k + 1$. Then, the input value y_j^l into neuron j in layer l is

$$y_j^l \equiv b_l + \sum_{i=1}^{p} a_i^{l-1} w_{ij}^{l-1,l} \tag{1.4}$$

where p is the number of neurons in layer $l-1$ and a_i^{l-1} denotes to the function value of the activation function for neuron i in layer $a_i^{l-1} = f(y_i^{l-1})$ [5, 6]. For example, the activation function can be defined as

1. sigmoid
$$f(x) = \frac{1}{1 + e^{-x}} \tag{1.5}$$
2. hyperbolic tangent
$$f(x) = \tanh(x) \tag{1.6}$$
3. Gaussian function
$$f(x) = e^{-ax^2} \tag{1.7}$$

Sometimes, the identity $f(x) = x$ activation function can be used, especially in situations, when a change of values is not wanted [6]. Commonly used activation functions are shown in Figure 1.3. The nowadays popular ReLu is not suitable for my purpose because has discontinuous differentiation.

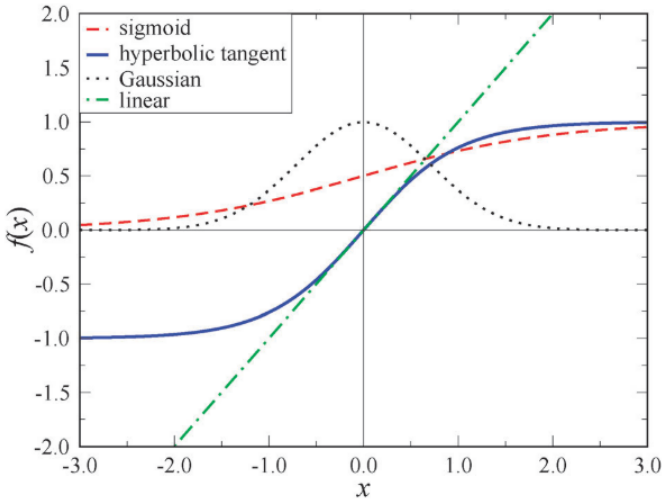

Figure 1.3: The summary of the often used activation functions. Figure taken from Ref. [6].

1.2.2 Learning algorithm

This section will focused on the process of learning itself. The basic principles of learning will be introduced. More advanced concepts of learning can be found in Ref. [4]. Usually data set is divided into two parts, the train part and the test part. A learning, and training data set is used for the process of learning, whereas a test set represents a source of unbiased information, which is not used during learning. In neural networks, the term learning is understood as a numerical process that edits the values of weights and biases throughout the entire neural network. This process allows for a gradually better prediction of the neural network employing the training dataset.

To compare the quality of the prediction, the so-called cost function is typically employed. This function can be described under various forms, see Ref. [4]. For the sake of explanation, here it will be described in its simplest form

$$C(w,b) = \frac{1}{2n}\sum_{x}\|y(x) - a\| \tag{1.8}$$

where $y(x)$ represents known information from data set and a refers to predicted value of our model, $\|.\|$ refers to the norm because generally vectors are used. The aim is to set the weighting and bias to minimize the cost function. The simplest way to minimize respectively find a local minimum of the function is through the gradient descent algorithm with respect to parameters w and b [4, 5]. This can be obtained by defining the following sequence

$$w_i \to w_{i+1} = w_i - \eta\frac{\partial C}{\partial w_i}$$

$$b_i \to b_{i+1} = b_i - \eta\frac{\partial C}{\partial b_i} \tag{1.9}$$

where indexes i and $i+1$ respectively refer to iterations steps and parameter η denotes the size of a step in the direction of the local minimum in multidimensional space. It can be shown, Ref. [5], that the best choice of parameter η is $\eta = \epsilon/\|\nabla C\|$, where $\epsilon > 0$ is denoting the desirable prediction error. The gradient descent method reflects the basic idea behind the search for optimal values of the weight and biases. Nowadays there exist many more advanced approaches to find a local minimum, such as *stochastic gradient descent* [4, 5], *Adam* [7] or Kalman filter [8].

The process of the cost function evaluation is called *forward propagation* [4]. The remaining question is how to compute gradients most efficiently and set new values of weights and biases. This process is called *back propagation*. It is important to mention that backpropagation is not a minimization method. It is just a way to efficiently compute gradients as a function of weight and bias for individual layers and neurons within layers.

Let's defined an error δ_j^l, which represents the influence of j-th neuron in l-th layer on the final value of the cost function C

$$\delta_j^l \equiv \frac{\partial C}{\partial y_j^l} \tag{1.10}$$

where y_j^l is from Equation (1.3). We can use this definition to calculate the error in output layer δ_j^L as

$$\delta_j^L = \frac{\partial C}{\partial a_j^L}\frac{\partial a_j^L}{\partial y_j^L} = \frac{\partial C}{\partial a_j^L} f'(y_j^L) \tag{1.11}$$

where $a \equiv f(y)$. The first part represents the sensitivity of the cost function to change in the j-th neuron output. The second term in Equation (1.11) accounts for the change in the activation function due to a change in input. Symbol L refers to the index of the output layer. We can rewrite this equation into vector form, where the vector has layer length.

$$\delta^L = \nabla_a C \odot f'(y_j^L) \tag{1.12}$$

where symbol $\odot$ stands for the Hadamard product, which is defined as the multiplication of two vectors with the same length element-wise, s and t are vectors and index j refers to the j-th element, then $(s \odot t)_j = s_j t_j$ [5]. Symbol ∇_a refers to partial derivative $\partial C/\partial a_j^L$.

Equation (1.10) works for errors in the output layer. The error in arbitrary layer δ^l can be expressed by means of error of following layer δ^{l+1}, then Equation (1.10) has following form

$$\delta_j^l = \frac{\partial C}{\partial y_j^l} = \sum_k \frac{\partial C}{\partial y_k^{l+1}}\frac{\partial y_k^{l+1}}{\partial y_j^l} = \sum_k \frac{\partial y_k^{l+1}}{\partial y_j^l}\delta_k^{l+1} \tag{1.13}$$

$$y_k^{l+1} = \sum_j w_{kj}^{l+1} a_j^l + b_k^{l+1} = \sum_j w_{kj}^{l+1} f(y_j^l) + b_k^{l+1} \tag{1.14}$$

where indexes k, j refers to neurons and indexes l denotes to layer. Thus

$$\frac{\partial y_k^{l+1}}{\partial y_j^l} = w_{kj}^{l+1} f'(y_l^j) \tag{1.15}$$

in the end

$$\delta_j^l = \sum_k w_{kj}^{l+1} \delta_k^{l+1} f'(y_j^l) \tag{1.16}$$

The equation can be rewritten with the usage of Hadamard product as

$$\delta^l = ((w^{l+1})^T \delta^{l+1}) \odot f'(y^l) \tag{1.17}$$

where $(w^{l+1})^T$ is transpose matrix of weights for $l+1$ layer. Multiplication with the transpose matrix $(w^{l+1})^T$ causes the transfer of the error through the neural network [5]. Using equations (1.12),(1.17) the error in an arbitrary layer can be estimated. The error in layer l can be calculated using the error in the output layer (1.12) by iterative calculation. The error in the $l+1$ layer is known, in first iteration $l+1 \equiv L$, then with usage of Equation (1.17), error is calculated in the l layer, then redefined $l \equiv l+1$ and iterate or backpropagate the error to the input layer

All the above-mentioned equations are used in the process of the calculation of the gradients of the cost function. For the biases

$$\frac{\partial C(f(y_j^l))}{\partial b_j^l} = \frac{\partial C}{\partial f(y_j^l)} \frac{\partial f(y_j^l)}{\partial y_j^l} \frac{\partial y_j^l}{\partial b_j^l} = \delta_j^l \tag{1.18}$$

and for the weights

$$\frac{\partial C(f(y_j^l))}{\partial w_{jk}^l} = \frac{\partial C}{\partial f(y_j^l)} \frac{\partial f(y_j^l)}{\partial y_j^l} \frac{\partial y_j^l}{\partial w_{jk}^l} = \delta_j^l a_k^{l-1} \tag{1.19}$$

The Equations (1.18) and (1.19) can be used for direct calculation of the gradient of a cost function using the defined error δ. Equations (1.12), (1.17), (1.18), (1.19) present the backpropagation method. The calculated values from the gradients can be used in minimization methods, such as gradient descent in Equation (1.9), and the newly estimated values of the weights and biases are then updated in the neural network.

The whole process of learning by backpropagation has the following steps

1. A train data from the data set are loaded into the input layer
2. For each training example
   (a) Feedforward process is applied using Equation (1.4) for each layer of NN.
   (b) The error in the output layer is calculated according to Equation (1.12).
   (c) The remaining errors of the NN are calculated by Equation (1.17).
3. The calculated values of the gradients used for the minimization method, such as gradient descent, and new values of the weights and the biases are obtained.

1.2.3 The evaluation of the machine learning prediction

The goal of machine learning models is to achieve the most accurate prediction on related data that were not used during the process of learning. The problem is that the learning process on the learning data can achieve theoretically arbitrary small values of error. This is the reason why the test data set is introduced. The model can have two limiting cases: *underfitting* and *overfitting*. Underfitting is a situation when the model has few fitting parameters and is not able to describe all relations between the data and eventually gives a poor prediction. On the other hand, when the model has too many fitting parameters, it can give a very good prediction on the training data but fails to give a good prediction for the testing data. As a toy model quadratic equation can be used, see Figure 1.4. In the Figure are three cases, on the left side we used a linear model to describe the data, unfortunately linear model poorly describes the data and we have an underfitted case. The right-hand side of this figure represents the case of an overfitted model. The training points are very well described but the model is not able to identify any new points with quadratic dependence. The ideal case is to use a second-order polynomial, which is shown in the middle of Figure 1.4

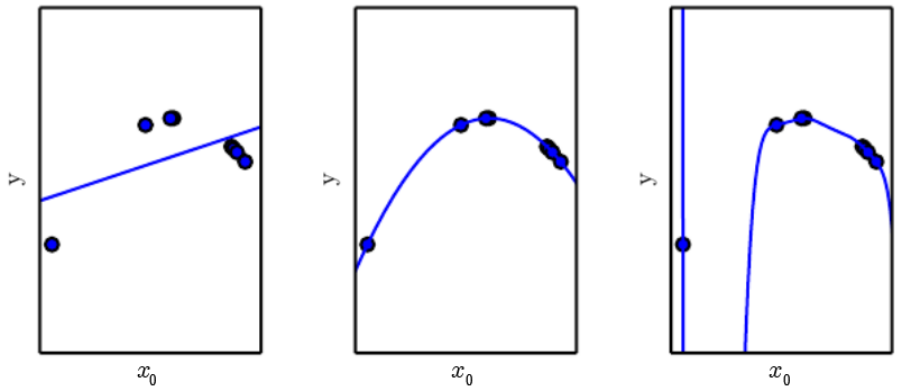

Figure 1.4: Difference between underfitting and overfitting. The left shows a case of underfitting, the middle shows a suitably chosen model and the right shows an example of overfitting. Figure taken from Ref. [4].

Several fitting parameters are called *capacity* [4].The capacity can be understood as the ability of a model to capture multidimensional functions. A typical relation between error on the train and test data depending on the capacity of a model is shown in Figure 1.5.

It is seen in Figure 1.5, that the error on the training data is asymptotically approaching zero, whereas the error of the prediction has a convex shape. The gap between training error and predicting error increases with the capacity of a model. The minimum of the generalization error refers to the optimal capacity of the model. Capacity values to the left of the optimal capacity correspond to the underfitted model, and capacity to the right of the optimal capacity refers to the overfitted model.

We need to take great care to set the neural network parameters correctly. The

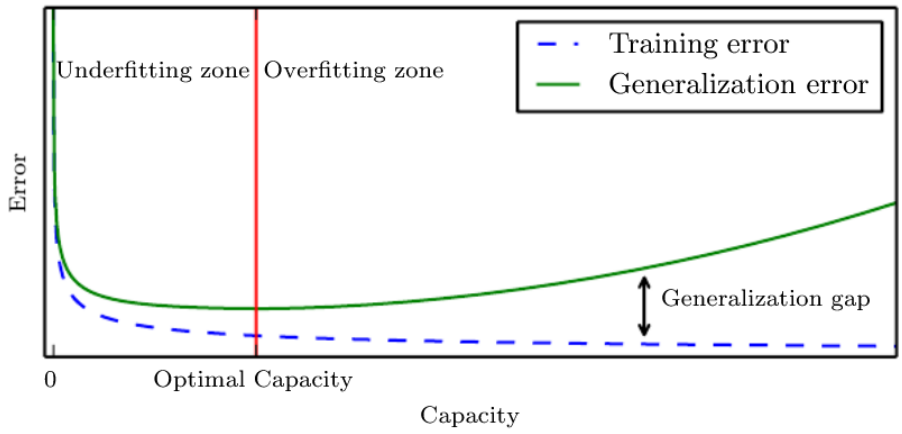

Figure 1.5: Typical relationship between model error on training data and general model error as a function of model capacity. To the left of the optimal capacity is the underfitting region and to the right is the overfitting region. Figure taken from Ref. [4].

quality of the prediction can be affected by capacity, type of the activation function, the minimization method, the quality of the data set, the way of creation of training and test data set, the initial set of the weights and the biases, the way of training and by the type of cost function. The number and the size of the layers represent the capacity of the model. By setting of all the above parameters we can improve or worsen the quality of the prediction of the neural network also these parameters should be set about the application and size of the data set.

1.3 Development of neural network interatomic potentials for molecular dynamics

This section will introduce the concept of using neural networks in developing the interatomic potential for molecular dynamics as well as the main problems and bottlenecks of this methods. Nowadays two major approaches in the creation of the machine learning interatomic potential are used. Neural networks and Kernel ridge regression.

Whereas neural networks decompose multidimensional nonlinear functions into a net of linear functions connected with a nonlinear activation function, the kernel-based method approximates this function by a linear combination of typically nonlinear functions known as a kernel [9]. Both methods can yield similar results but Kernel-based methods are more suitable for small data sets because the learning procedure can be computationally consuming due to the number of training points. A rule of thumb could be to prefer kernel methods when there are less than $10^3 - 10^4$ training points [9].

Quality and generality of a machine learning model mainly depend on the data set, which usually contains structure coordinates, energy of atoms, and acting forces. Machine learning models have no analytical expression of fitted function, therefore the physics of the system is dictated by the data set. Machine learning models representing a potential energy surface are usually based on the idea of decomposition of the total energy into summation over the energies of all elements in the system.

$$E_{\text{tot}} = \sum_i E_i(\vec{R}) \tag{1.20}$$

where E_i, the energy of a i-th atom, depends on the chemical environment of the atoms defined by the positions of all neighbors inside some sphere with cutoff radius R_{c} [6]. The first application of the use of neural networks for potential energy prediction struggled with the description of the structural input for the NN and with the dependency of the system size on the results. These problems will be discussed in the following sections and I will introduce solutions to the problems within the Behler - Parrinello frame [10].

1.3.1 High-dimensional neural network potentials

The neural network is constrained by the size of the input layer once the model is trained. Thus, any change in the degrees of freedom of the input layer would make the fitted model useless for prediction and a new neural network has to be fitted. Based on this, it is not possible to simply add a new node to the input layer with a newly added atom. The second drawback is that the standard feed-forward neural networks are dependent on the order in which the data are loaded into the input layer. When two chemically and physically same atoms are exchanged, nothing would happen from the physical point of view, but this does not apply to a neural network. In 2007 Behler and Parrinello introduced the method how to overcome

this limitation [10]. They took advantage of Equation (1.20) and replaced the neural network representing the total energy with a set of atomic neural networks [10, 11]. Each atomic neural network gives contribution E_i which is used in summation of the total energy from Equation (1.20).

The construction of an atom-based high dimensional neural network is schematically shown in Figure 1.6. Initially, each atom in the system is described by Cartesian coordinates $\vec{R}_i = (X_i, Y_i, Z_i)$. Cartesian coordinates are then transformed into a suitable set of internal coordinates for the atomic neural network. This internal set of coordinates represents the environment of an atom within the cut-off radius.

In this work, I will use the symmetry functions presented in Ref. [10, 11]. Symmetry functions set consists of fixed number of functions M_i for each element i which describes the environment; $\vec{G}_i = \{G_{i,j}\}$ where $j = \{1, ..., M_i\}$. This set of symmetry functions is used as an input for the atomic neural network and the atomic energy contribution to the total energy is estimated. Figure (1.6) also shows, that by adding or removing the atom in the system it just adds or removes an atomic neural network. In the end, this means that this approach overcomes the size-dependent problem. The above-mentioned architecture of the atomic neural network is made for each chemical element, due to this fact computational effort increases with the number of elements in a system. For example, for the atomic neural network with two neurons

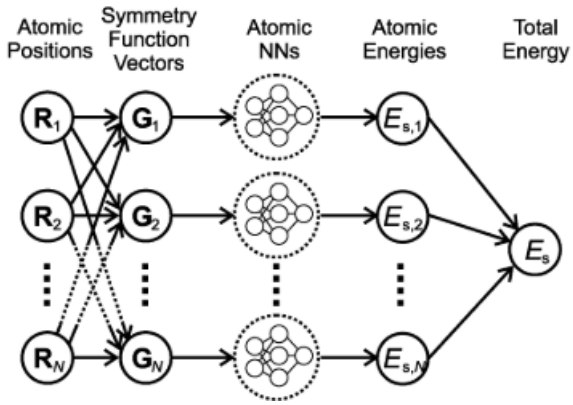

Figure 1.6: Schematics of the architecture of a high-dimensional neural network. The positions of individual atoms $\vec{R}$ are used to describe the neighborhood of an atom using a set of symmetric functions G_i, where i represents the indexing of the neighborhood of each atom. The set of symmetric functions is also the input layer for the feed-forward neural network. The total energy E_{tot} is the sum of the predictions of the individual networks. Figure taken from Ref. [6].

in each layer, three hidden layers, and an atomic environment described by four symmetric functions, we obtain atomic energy contribution as

$$E = f_1^3(b_1^3 + \sum_{l=1}^{2} w_{l1}^{23} f_l^2(b_l^2 + \sum_{k=1}^{2} w_{kl}^{12} f_k^1(b_k^1 + \sum_{j=1}^{4} w_{jk}^{01} G_j))) \tag{1.21}$$

where f represents activation functions. The usual architecture of an atomic neural network has two or three hidden layers each containing from 25 to 40 neurons [6].

The acting forces can be calculated as a derivative of estimated energy as follows

$$F_{k,\alpha} = -\frac{\partial E}{\partial R_{k,\alpha}} = -\sum_{i=1}^{N} \frac{\partial E_i}{\partial R_{k,\alpha}} = -\sum_{i=1}^{N}\sum_{j=1}^{M_i} \frac{\partial E_i}{\partial G_{ij}} \frac{\partial G_{ij}}{\partial R_{k,\alpha}} \tag{1.22}$$

where $F_{k,\alpha}$ is force action on k-th atom with coordinates $\alpha = \{x, y, z\}$, M_i is the number of symmetry function describing environment of i-th atom and N is the number of atoms. The first term in equation $\frac{\partial E_i}{\partial G_{ij}}$ is given by the architecture of the neural network, the second term is given by the definition of the symmetry function $\frac{\partial G_{ij}}{\partial R_{k,\alpha}}$.

The calculated forces from DFT can be used in the learning process and the model can predict them in the same way as the energy. Such a use enforces the normalization of the forces in the cost function. The forces are scaled by a factor, see Ref. [12]. The models using this approach predict the forces much more accurately than those learning only with the energies. On the other hand, correlation and causality between the energy and the forces are not ensured. Small partitions of the calculated forces can be used during the learning process. However, the number of used forces has to be determined with care.

1.3.2 Atom-centered symmetry functions

Cartesian coordinates are not the best choice for structural description. The main reason is that the neural network output depends on the absolute values of the input coordinates. Imagine an isolated system of the atoms described with Cartesian coordinates. When we apply translation or rotation operation on the system, energy does not change but every atom in the system has different Cartesian coordinates, thus the prediction of the neural network would be different due to different inputs. A straightforward solution is to describe the structure using internal coordinates such as interatomic distances. While this works well for small systems, the choice is not unique and their number grows rapidly with the size of the system [11]. Behler introduced the atomic-centered symmetry function which overcame the problem of translation and rotation. These functions describe the environment of the atom within a defined sphere with the center in that atom. For example, the sphere is described by a cut-off function that can by defined as

$$f_c(R_{ij}) = 0.5(\cos\left(\frac{\pi R_{ij}}{R_\mathrm{c}}\right) + 1) \quad R_{ij} \leq R_\mathrm{c}$$

$$f_c(R_{ij}) = 0 \qquad\qquad R_{ij} > R_\mathrm{c} \tag{1.23}$$

where R_{ij} is distance between atoms i, j and R_c is radius of the sphere. This function decreases to zero when approaching to R_c, which reflects the influence of further atoms on the atom in the center. The problem with such a cut-off function is the discontinuity of the second derivative at the cutoff radius [11]. This discontinuity can cause errors in molecular dynamics simulation, but this limitation can be overcome with a sufficiently large cutoff [11]. Symmetry functions are multiplied by the cutoff

function so the atoms out of the sphere do not contribute to the description of the environment and thus to the prediction of the energy.

The last limitation for the symmetry function is its differentiability and analytical form of differentiation. The request originates in Equation (1.22), where we need differentiation of the symmetry function to obtain forces. The atomic-centered symmetry function is divided into two parts. The radial symmetry function which describes two-body interaction and the angular symmetry function represents three-body interaction. Three examples of symmetry functions (G_1, G_2, G_3) are shown below

$$G_i^1 = \sum_j f_c(R_{ij}) \tag{1.24}$$

where index j describes all atoms within the cutoff radius R_c and index i refers to the atom in the center of the atom sphere.

$$G_i^2 = \sum_j e^{\eta(R_{ij}-R_s)^2} f_c(R_{ij}) \tag{1.25}$$

function G^2 is base on Gaussian function of a width η and s shift R_s

$$G_i^3 = \sum_j \cos(\kappa R_{ij}) f_c(R_{ij}) \tag{1.26}$$

The symmetry function G^3 should not be used alone but in combination with other symmetry functions. The G^3 symmetry function is similar to the description of the environment by Fourier series with parameter κ [11].

Angular symmetry functions can have the following description

$$G_i^4 = 2^{1-\zeta} \sum_{j,k\neq i} (1+\lambda\cos(\Theta_{ijk}))^\zeta e^{-\eta((R_{ij}-R_s)^2+(R_{ik}-R_s)^2+(R_{jk}-R_s)^2)} f_c(R_{ij}) f_c(R_{ik}) f_c(R_{jk}) \tag{1.27}$$

$$G_i^5 = 2^{1-\zeta} \sum_{j,k\neq i} (1+\lambda\cos(\Theta_{ijk}))^\zeta e^{-\eta(R_{ij}-R_s)^2+(R_{ik}-R_s)^2} f_c(R_{ij}) f_c(R_{ik}) \tag{1.28}$$

where parameter λ is equal to -1 or 1, parameter ζ refers to curvature of the symmetry function. The function G^4 describes the interaction between all three atoms ijk, while function G^5 describes the interaction between centered atoms i with atoms jk determined by angle Θ_{ijk} [11].

Because the value of symmetry functions can range widely, it is convenient to scale or center them due to numerical reasons. Such a scaling can be simply done by

$$G_\mathrm{scaled} = \frac{G - G_\mathrm{min}}{G_\mathrm{max} - G_\mathrm{min}} \tag{1.29}$$

and centering

$$G_\mathrm{scaled} = G - G_\mathrm{average} \tag{1.30}$$

if both scaling and centering are applied

$$G_\mathrm{scaled} = \frac{G - G_\mathrm{average}}{G_\mathrm{max} - G_\mathrm{min}} \tag{1.31}$$

where G_{min}, G_{max}, G_{average} represents the minimal or maximal value of a particular symmetry function respective to its average.

All symmetry functions are based on the summation of all atoms in the particular cut-off sphere. The advantage of this summation is the independence of the number of atoms in the sphere around the central one. On the other hand, information about the initial structure is lost. Thus the transformation from Cartesian coordinates to atom-centred symmetry function is not bijection and it cannot reproduce original Cartesian coordinates from a given set of symmetry functions. Great care is needed to take on setting symmetry function sets and try to avoid the situation, where two different structures are described by the same symmetry function set but have different energies. It is common to use more symmetry functions with different parameters to ensure a unique relation between the symmetry function set and the energy. For radial symmetry functions, it is common to calculate the second differentiation concerning parameter η in equation (1.25) and find the value of η_{min} where the second derivative is zero. Then create an equidistant mesh of values from zero to determined value η_{min}.

For angular symmetry function, it's common to set its parameters as $\eta = 0$, $\lambda = \pm 1$, $\zeta = 1, 2, 3, 4, 16$. This initial guess usually ensures a sufficient description of structures. The influence of the parameters on the shape of radial and angular symmetry functions is shown in Figures 1.7 and 1.8. In the latter figure, note can be seen that the symmetry function with parameter $\lambda = \pm 1$ causes sampling to go through all angles.

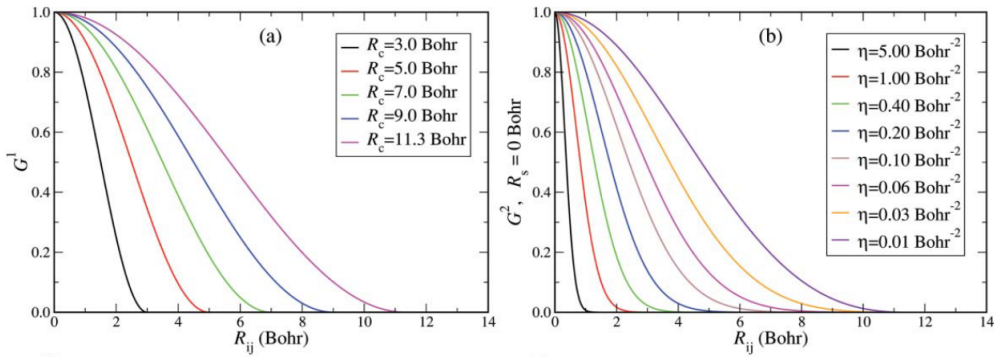

Figure 1.7: (a) Influence of R_{c} on the shape of cut-off function, (b) Equidistant sampling of radial symmetry functions concerning parameter η. Figures taken from Ref. [11].

1.3.3 Extrapolation and interpolation

The quality of the prediction of the machine learning potential strongly depends on the number of extrapolations and interpolations.

Extrapolation occurs when the model is forced to predict data beyond the known data from the data set. In such cases, the model can give us very poor or unreliable predictions and the data has to be presented with care. On the other hand, interpolation is a situation when the dataset is poorly sampled and the model has a poor

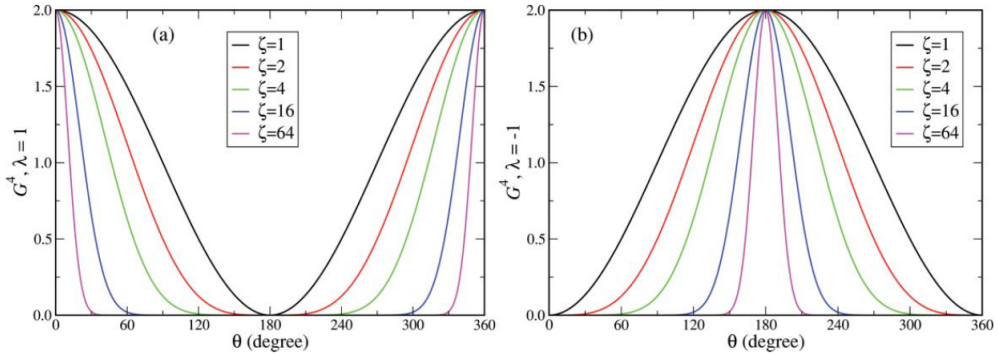

Figure 1.8: (a) Influence of parameter ζ for $\lambda = 1$, (b) Influence of parameter ζ for $\lambda = -1$. Figure taken from Ref. [11].

prediction.

The occurrence of the extrapolation is easy to detect. It is known, what the data set looks like and it is not hard to detect when the model goes out of the data set range. The more problematic is the detection of the interpolations. It is hard to detect the regions of poor sampling. The convenient way, how to detect the interpolation is to create more machine learning models of the same methodology with different capacities (e.g. number of neurons). If the models predict very differently on particular data points, it means, that such a data point is poorly sampled and needs to be added into the data set.

In general, the goal is to reduce the extrapolation and interpolation by sufficient sampling of the data set and by the diverse dataset.

1.4 Shape memory alloys

Shape memory alloys (SMA) are widely studied materials due to their reversible martensitic microstructural transformation that leads to extraordinary mechanical properties. SMAs are also of great industrial interest because of their application in the biomedical, aerospace, or automotive industries. The phase transformation is usually between the parent phase, which appears at high temperature, and the martensitic phase, a lower temperature phase. The reversible martensitic transformation causes the two main features of the SMAs: shape memory effect and superelasticity.

The martensitic transformation in materials is a very complex problem that demands an investigation on all possible theoretical levels, from DFT calculation through multiscale models in molecular dynamics to continuous models [1, 13]. A frequently used method for experimental observation of martensitic transformation is transition electron microscopy. Nowadays transition electron microscopy provides high-resolution imaging reaching the atom level but only artifacts of the transformation can be seen and guessing the processes backward is challenging. Theoretical approaches, such as DFT can offer us an insightful view on a microscopic level, but the calculations are constrained by the ground state which is not suitable for modeling processes such as shape memory effect because these effects are usually coupled with temperature. Methods such as ab-initio molecular dynamics could be alternatives but we are limited by the size of the supercell and the computations can be demanding. The last computational technique to observe the time evolution of a system on an atomic level is MD, which seems suitable for such a task, but usually, the available interatomic potentials are not able to capture the complexity of the martensitic transformation.

Even though SMAs have been intensively studied for over a half of century, many problems remain. During the martensitic transformation, the system can undergo plastic deformation via dislocation movement in specific slip systems and defects can be created which can lead to loss of reversibility and ultimately loss of the unique mechanical properties. In this work, we will focus on the mostly studied alloy Nickle - Titanium (NiTi) which is well known for its good transformation reversibility, and biocompatibility and is mostly used in SMA applications.

1.4.1 Shape memory and superelasticity

The shape memory effect is the ability of a material to recover its original shape after a large (several percent) inelastic deformation. At temperature below M_f the system is in self-accommodated twinned martensite, when an external stress is applied, the structure becomes fully detwined, which remains so upon unloading. Heating the unloaded detwinned martensite above A_f would transform it into a parent phase called austenitic which can return to the original twinned martensite by cooling.

Superelasticity is the isothermal effect above A_f temperature. It enables material full recovery after inelastic strain. Through stress underloading, the austenitic phase

is transformed to detwinned martensite and during unloading, the microstructure is reverted into austenite [13]. These processes are shown in Figure 1.9. The path

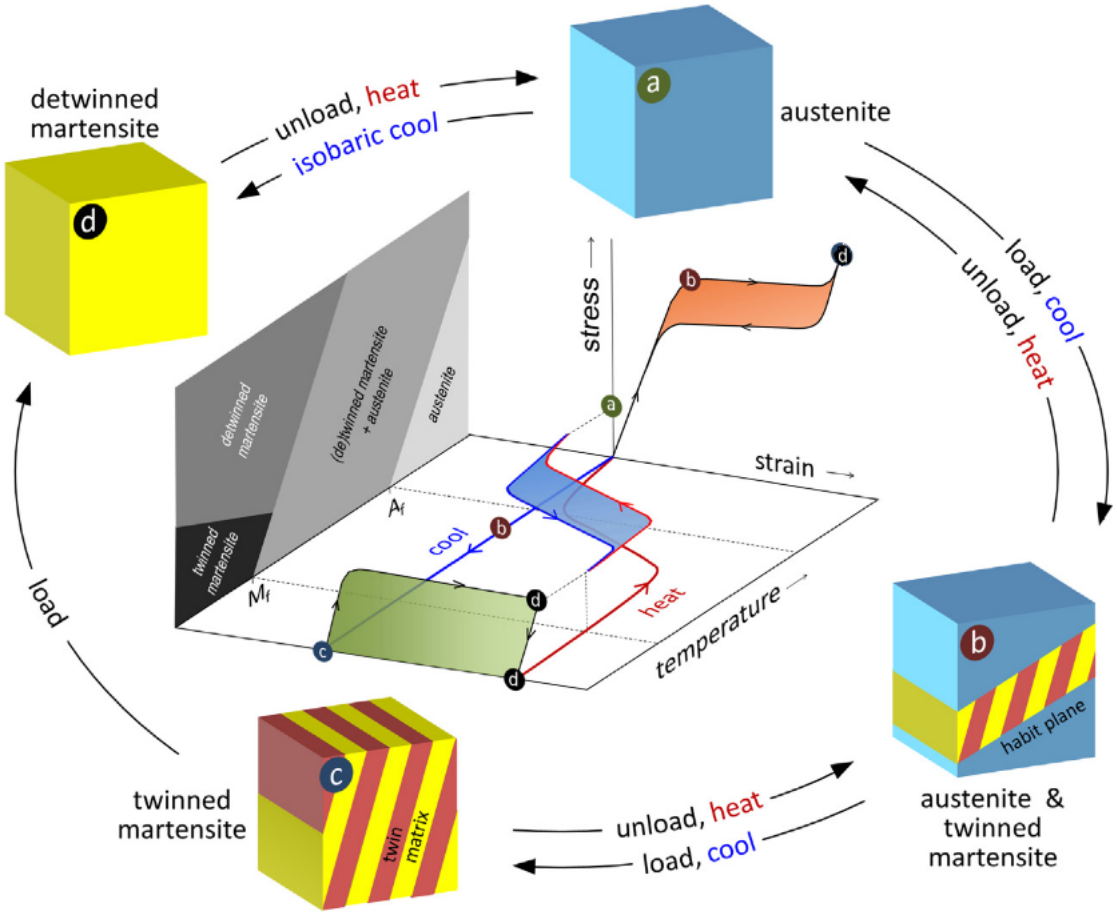

Figure 1.9: Phase transformations during shape memory effect (path c - d - a-c) and superelasticity (path a - b - d - a). Figure taken from Ref. [13].

from twinned martensite (c) through fully detwinned martensite (d) and austenite (a) back to twinned martensite represents the shape memory effect. Superelasticity above temperature A_f is defined by the path from austenite (a) to detwinned martensite (d) back to austenite (a).

1.4.2 Martensitic transformation

The martensitic transformation is a diffusionless phase transformation in solids, in which atoms move cooperatively, and often by a shear-like mechanism [14]. The martensitic transformation is divided into two main groups, weak transformation and reconstructive transformation [15–17]. Weak transformation is a process in which the symmetry group of both the parent and product phase is included in a common finite symmetry group whereas reconstructive transformation occurs otherwise [15]. The idea behind reconstructive phase transition can be shown by a 2D model square-to-hexagonal phase change. Let's assume a square lattice, as it is shown on the left side of Figure 1.10. This cell is transformed into the unit cell of the hexagonal lat-

tice. Based on symmetry, it can establish a new dashed unit cell that is equivalent. The new dashed unit cell can be transformed back into the squared lattice, which is shown on the right side of Figure 1.10. The same squared lattice is observed, however the original unit cell (marked with a solid line) is sheared. It means that during the

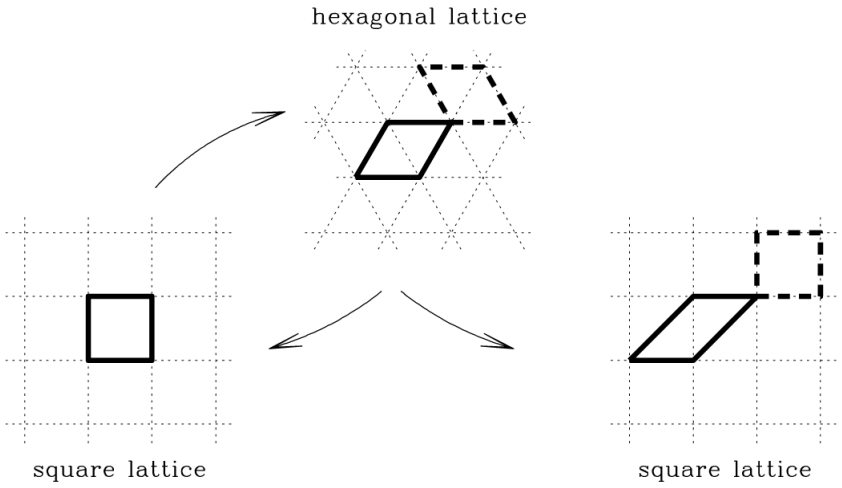

Figure 1.10: A lattice-invariant shear generated by a forward and reverse square-to- hexagonal phase transformation. Figure taken from Ref. [15].

transformation, applying symmetry operation and transforming back, we have deformed the crystal through a lattice-invariant shear [15]. Because the squared lattice are the same, as they represent the same lattice, the energy surface of the crystal has infinitely many wells regarding infinitely many same lattices. The shape of the energy landscape is determined by Landau's theory of phase transition [18]. For reconstructive martensitic transformation, the energetic barrier between the infinitely many energy wells of the crystal is at most equal to that of the underlying transformation. Based on mathematical theory it can be shown that any reconstructive transformation necessarily generates unbounded distortion which in the end leads to the irreversible phase change [15]. A deeper discussion is out of the scope of this work, see Ref. [15, 19, 20].

The energetic landscape of the weak and reconstructive martensitic transformation is shown in Figure 1.11. Figure 1.11 (a) is an energy landscape of reconstructive transformation in the square-to-hexagonal lattice, where s denotes to square phase and h denotes to hexagonal one. Figure 1.11 is an energy landscape of the weak square-to-rhombic martensitic transformation. The squared state s in metastable and new minima appeared at intermediate rhombic configuration r. The Erricksen-Pitteri neighborhood (EPN) of the weak martensitic transformation refers to the part of the energy landscape that does not contain any lattice-invariant shears. Thus, contains only a finite number of energy wells [15]. Alternatively, it is a neighborhood beyond the set of martensitic lattices related to the reference lattice of austenite by unique lattice correspondence resulting from the transformation path [21]. This above-mentioned fact has the following implication: Reconstructive transformations are accompanied by plastic deformation through dislocation and twinning in the parent phase that leads to the irreversibility of the phase transition.

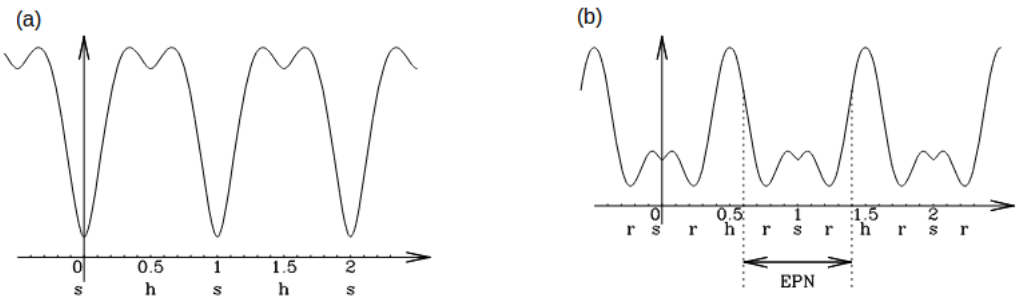

Figure 1.11: The r denotes rhombic, s to squared, and h to hexagonal, (a) the energy profile of square-to-hexagonal reconstructive transformation along the s-h-s line; (b) the energy profile of a crystal close to square-to-rhombic transformation, along the s-r-h line with metastable square state s. Figure taken from Ref. [15].

1.4.3 NiTi

NiTi is one of the most studied shape memory materials due to its considerable technological relevance. The martensitic transformation in NiTi undergoes between low symmetry, low-temperature martensitic B19' structure, high-symmetry, high-temperature austenitic B2 structure. The martensitic diffusionless phase transformation between B2 and B19' has been extensively studied in the past decades and the mechanisms of the plastic deformation during the transformation are relatively well described, see, e.g., Refs. [13, 22]. Although the martensitic phase transformation of near equiatomic NiTi should be fully reversible because of the group-subgroup relation for the weak martensitic transformation, as was proposed by Ref. [15], defect generation is still observed. The defects cause degradation of the superelasticity and shape memory effect shown in Figure 1.12. To investigate the mechanisms be-

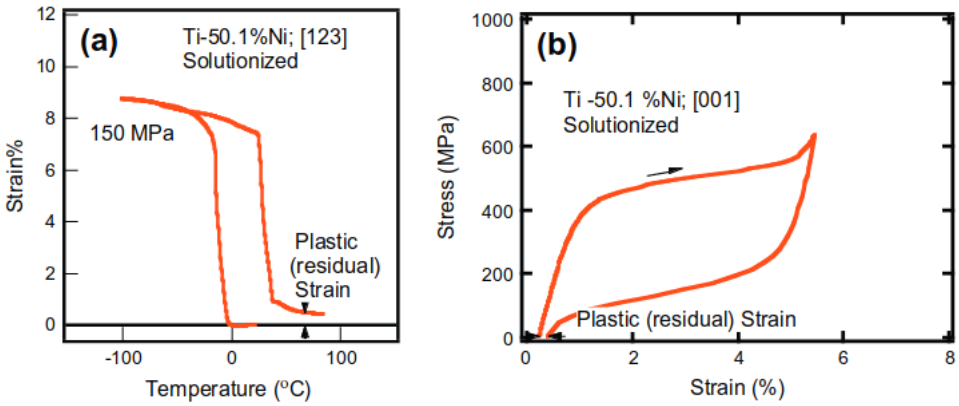

Figure 1.12: Shape memory and superelasticity experiments on solutionized 50.1 % Ni–Ti: (a) Macroscopic plastic residual strain upon temperature cycling under constant stress, (b) the plastic residual strain at constant temperature (T = 28 °C). Figures taken from Ref. [22].

hind plastic deformation, dislocation slip systems in austenite have been extensively studied on both experimental and theoretical levels. Detailed atomistic study of energetically favorable slip system is presented in Ref. [22]. The authors of Ref. [22]

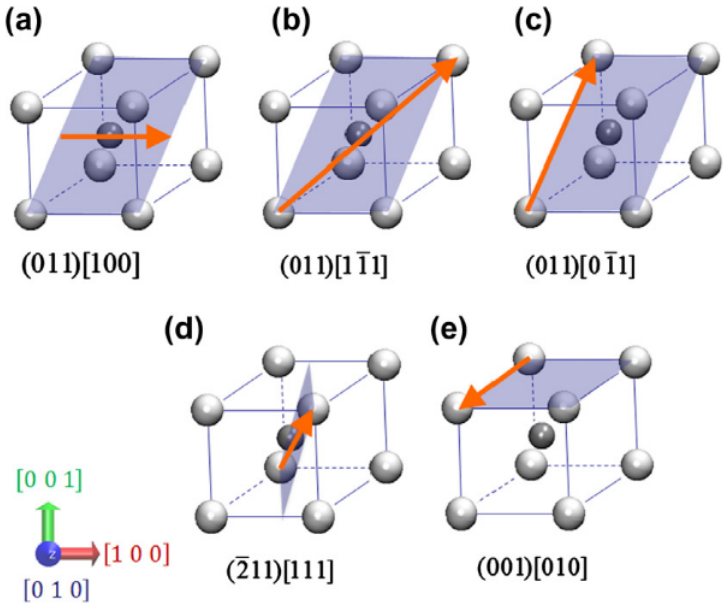

Figure 1.13: Different possible slip system in austenitic NiTi. The grey array denotes to slip plane and the arrow shows the slip direction. Figure taken from Ref. [22].

calculated based on the DFT theory the generalized stacking fault energy (GSFE) [23] for the {011}, {$\bar{2}$,1,1} and {001} planes in <100>, <111> and <011> directions in B2 austenite. The combination of all possible slips in austenitic NiTi is shown in Figure 1.13. The calculations show that the (011)[100] and (011)[1$\bar{1}$1] (here (...) and [...] denote slip plane and slip direction, respectively) systems are energetically favorable over other slip systems. This is in agreement with experimental observations.

Despite a detailed study of plastic deformation in austenite, the occurrence of defects such as $(41\bar{1})_P$ twins which have origin in $(20\bar{1})_M$ (subscript P and M denote to parent phase and martensitic phase, respectively) was still a mystery. Formation of $(20\bar{1})_M$ twins were usually observed in the martensitic phase after straining beyond recoverability limits, see Ref. [24]. These twins are not predictable by the classical

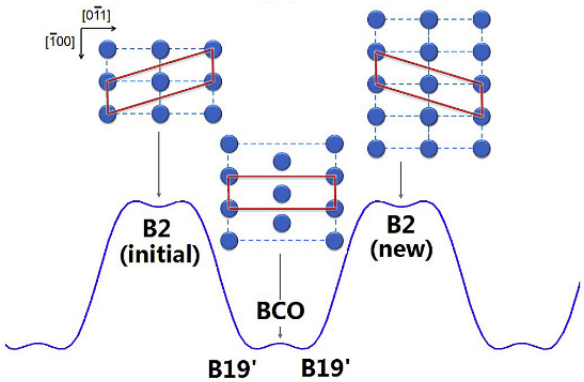

Figure 1.14: The merge of two EPN of two different austenitic B2 structures related through lattice invariant shear. The two EPNs are separated by a high symmetry structure refers to based centred orthorhombic structure(BCO). Figure taken from Ref. [19].

mathematical theory of martensitic microstructures as they correspond to straining conditions beyond the given EPN [1]. Straining beyond the given Eriksen-Pitteri neighborhood was first discussed by Gao et al. in Ref. [19, 20]. Assume two austenitic B2 structures which are related through a lattice invariant shear. Each B2 structure has its own EPN which can be connected into one energetic landscape as illustrated in Figure 1.14. To assume the connection between energetic landscapes, the existence of a related high-symmetry structure is needed, the existence of such a structure will be discussed later. The high symmetry structure should be metastable and create an energetic barrier between two EPNs. However, through the shear strain, the

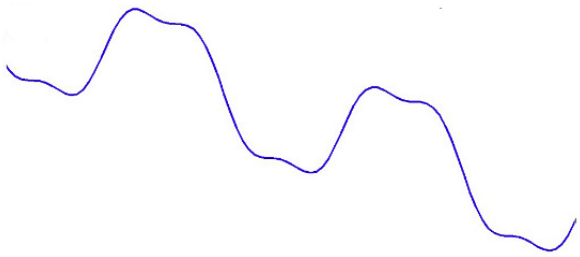

Figure 1.15: Free energy landscape of merged EPN under shear strain. Straining causes the vanishing of the energetic barrier of metastable high symmetry structure and creates a single energetic well. Figure taken from Ref.[19].

energetic landscape is distorted in a way that the energetic barrier between two EPNs vanishes and the transition becomes barrierless. What is more, shear strain can create a single energetic well as it is shown in Figure 1.15. This phenomenon is called a symmetry-dictated non-phase transformation pathway [19].

As was already mentioned the interconnection of two EPNs lies in the presence of a high symmetry structure. At the beginning of the century was surprisingly found that the B19' is not an energetic ground state. Theoretical calculation based on DFT showed that the base-centered orthorhombic structure B33 is more energetically favorable than B19', see Ref. [25]. However, the B33 structure was never experimentally observed. The fact that B19' is more favorable over B33 despite B33 having lower potential energy is usually justified by the free energy of the system. The act of temperature causes instability and in the end, other structures are more stable even though it has higher potential energy. Another feature in favor of B33 as a transient state between two EPNs is the existence of two crystallographically equivalent B2 states. Thus one B33 can be in both EPNs of different B2 structures as shown in Figure 1.14.

Results and discussion

In this section, I will introduce the method employed to construct an NN potential for B19' NiTi that produces consistent results with DFT and experiments. Prior to this, I will discuss the development of an NN potential for silicon, which served me as a proof-of-concept model. I will establish basic physical properties such as elastic constants and the phonon dispersion. The computational results predicted by the NN potentials will be compared to those obtained from existing analytical potentials and experimental data.

The data set will be generated by means of DFT simulations using the VASP code [26–28]. The NN potential will be fitted by the program RuNNer [29, 30]. All MD simulations are run under the LAMMPS code [31, 32]. The implementation of the fitted neural network for predicting the interatomic forces in MD systems is carried out using the n2p2 package [8, 33].

2.1 Proof-of-concept: Neural network potential for silicon

The aim of this part is not to create the most accurate potential but to demonstrate the generality and applicability of the NN potential model in the context of MD simulations. The created potential will be compared to the already existing analytical Tersoff potential which is presented in Ref. [34].

2.1.1 Basic properties of silicon

Silicon crystals naturally form under the diamond structure with a lattice parameter $a = 5.43$ Å. The space group of Silicon is 227 (F d-3m) and the primitive cell contains two atoms. The primitive lattice vectors are

$$\vec{a}_1 = \frac{a}{2}\hat{x} + \frac{a}{2}\hat{y} \qquad \vec{a}_2 = \frac{a}{2}\hat{x} + \frac{a}{2}\hat{z} \qquad \vec{a}_3 = \frac{a}{2}\hat{y} + \frac{a}{2}\hat{z} \tag{2.1}$$

where $\hat{x}, \hat{y}, \hat{z}$ refers to unit vectors of the orthogonal coordination system. The positions of the two basis atoms are given in fraction coordinates concerning the lattice

constant by

$$\vec{B}_1 = (0, 0, 0) \qquad \vec{B}_2 = (0.25, 0.25, 0.25) \tag{2.2}$$

I will further assess the quality of the potential through elasticity tensor C_{ijkl} which describes the elastic properties of the material. The linear stress-strain relation can be written in tensor notation as

$$\sigma_{ij} = c_{ijkl}\epsilon_{kl} \tag{2.3}$$

where σ_{ij} represents stress and ϵ_{kl} denotes to the infinitesimal strain tensor. Because diamond-structured silicon is a cubic crystal, the elasticity tensor has only three independent values $C_{11} = C_{22} = C_{33}$, $C_{12} = C_{21} = C_{31} = C_{32} = C_{13} = C_{23}$ and $C_{44} = C_{55} = C_{66}$, according to the Voight notation. The rest of the values are zero due to the symmetry of the crystal. Following the experimental measurements presented in Ref. [35], the elastic constants at room temperature are C_{11} = 165.64 GPa, C_{12} = 63.92 GPa, and C_{44} = 79.51 GPa. Then, the elasticity tensor reads (values are in GPa)

$$\begin{pmatrix} 165.64 & 63.92 & 63.92 & 0 & 0 & 0 \\ 63.92 & 165.64 & 63.92 & 0 & 0 & 0 \\ 63.92 & 63.92 & 165.64 & 0 & 0 & 0 \\ 0 & 0 & 0 & 79.51 & 0 & 0 \\ 0 & 0 & 0 & 0 & 79.51 & 0 \\ 0 & 0 & 0 & 0 & 0 & 79.51 \end{pmatrix} \tag{2.4}$$

2.1.2 Data set for the neural network potential

To train the NN potential, I constructed a data set that contains 752 structures of conventional cells with eight atoms. To ensure thermal fluctuations in all directions, some of these structures were obtained from an MD simulation of Si following NPT conditions at T = 300 K and P = 0 bar using the Tersoff potential from Ref. [34]. The data set also contains structures in which the atoms were randomly displaced up to 0.2 Å, structures in which the cell was compressed up to 2%, and structures which were sheared up to 0.5% in (001)[100], (100)[001], and (100)[010] directions. The

Table 2.1: Dependence of the calculated energy per atom of silicon on the plane-wave basis size.

plane-wave basis [eV]	energy [eV]	plane-wave basis [eV]	energy [eV]
250	-5.39876685	550	-5.42216369
300	-5.41172667	600	-5.42218459
350	-5.41902081	650	-5.42223646
400	-5.42114846	700	-5.4222662
450	-5.42205728	750	-5.42227147
500	-5.42219311	800	-5.42225724

resulting energies and forces for each structure were calculated by DFT. Brillouin zone was sampled employing the Monkhorst Pack net with 11 k-points in each direction of the reciprocal lattice and the size of the basis was set to 500 eV. In my DFT calculations, PAW PBE potential for silicon was adopted. The final parameters were set based on the convergence with different plane-wave basis sets and different densities of points in the first Brillouin zone. The dependence of the energy per atom on the plane-wave basis is shown in Table 2.1. It is sufficient to achieve an accuracy of 1 meV per atom because such accuracy is limited by the neural network fit itself. The energy values from Table 2.1 are plotted in Figure 2.1. The relation between the

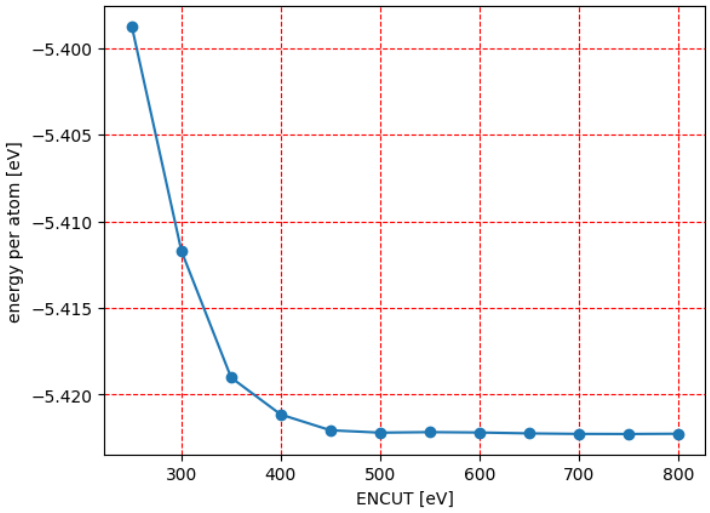

Figure 2.1: Relation between the energy per atom and the size of the plane-wave basis referred to as ENCUT.

number of k-points in the Brillouin zone and the energy per atom is shown in Figure 2.2. Note in Figure 2.2 that although the energy values fluctuate, all deviations are under the threshold of 1 meV per atom,

2.1.3 Neural network potential

The potential was fitted by the RuNNer code. For the atomic environment description, atom-centered symmetry function see equation (1.25) and (1.27) for radial respectively angular symmetry function. In total 26 radial and angular symmetry functions were used. The radius of the cut-off sphere was set to 6.36 Å and the cut-off function was identical to the equation (1.23). The neural network used to calculate the interatomic forces during an MD simulation consists of two hidden layers, each containing 10 neurons. The hyperbolic tangent activation function is adopted. For the output layer, however, the linear activation function is employed. The test dataset was 10% of the whole dataset and during the learning 10% of forces were used. I used 30 epochs to train the neural network. The Kalman filter was used as the training algorithm [8, 33]. A detailed description of all symmetry functions and the setup is in the Attachment of this work. The root mean squared

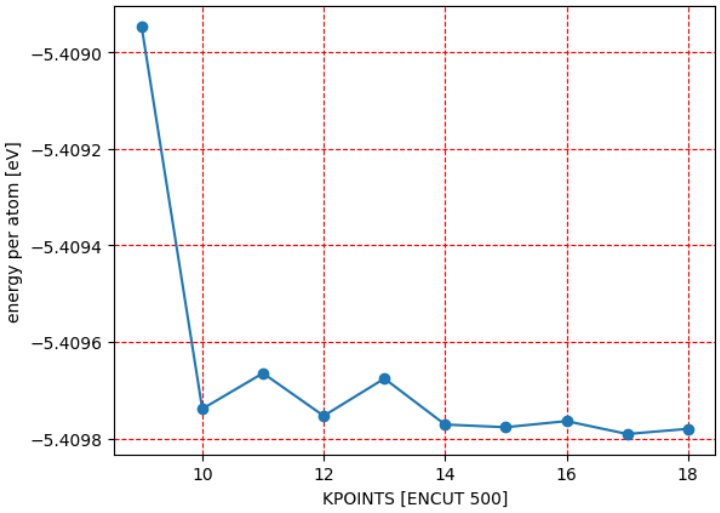

Figure 2.2: The relation between sampling of the Brillouin zone and the calculated energy per atom. The number on the x-axis represents the number of k-points used in the sampling for each direction of the reciprocal space.

error (RMSE) cost function is adopted

$$\text{RMSE} = \sqrt{\frac{\sum_{i=1}^{N}(x_i - \hat{x}_i)^2}{N}} \tag{2.5}$$

where N is number of inputs, x_i is the reference value and $\hat{x}_i$ is the value predicted by the model. Figure 2.3 shows the distribution of the energies per atom across the dataset. The energies are distributed within a reasonable range that varies from

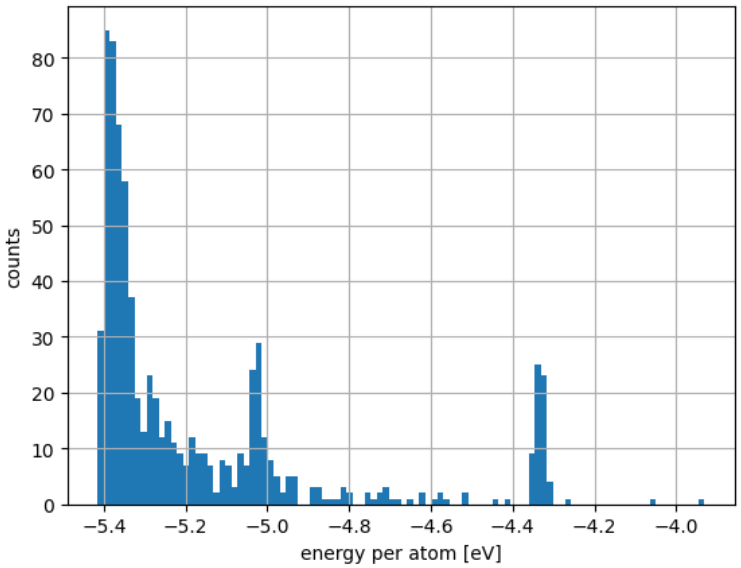

Figure 2.3: Distribution of energy per atom values from the dataset.

-5.4 eV to -3.9 eV. The lowest energies denote states around 300 K obtained from MD and the shearing of the cell. The highest energies come from the random atom

displacements imposed to the cells. It is important for the quality of the fit that the data set is sampled sufficiently. In addition, Figure 2.4 shows the evolution of the prediction error for the energies. The prediction error of energy smoothly decreases

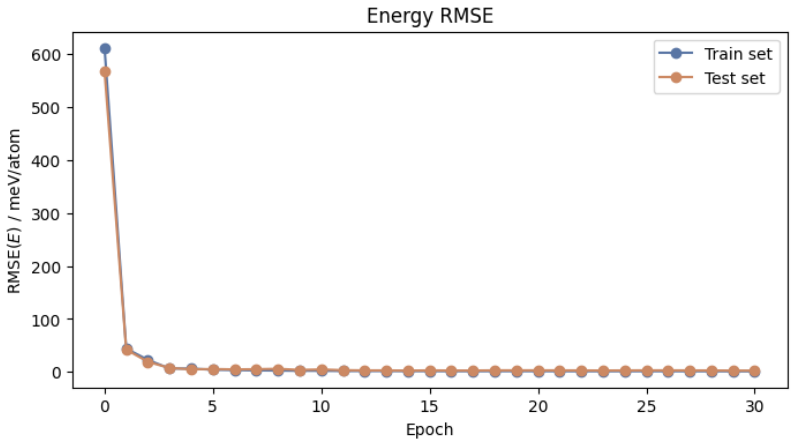

Figure 2.4: Evolution of energy prediction error during the process of training.

for both the training and test data. In Figure 2.5, the evolution of forces error prediction. The error also converges. The best prediction is observed at the epoch

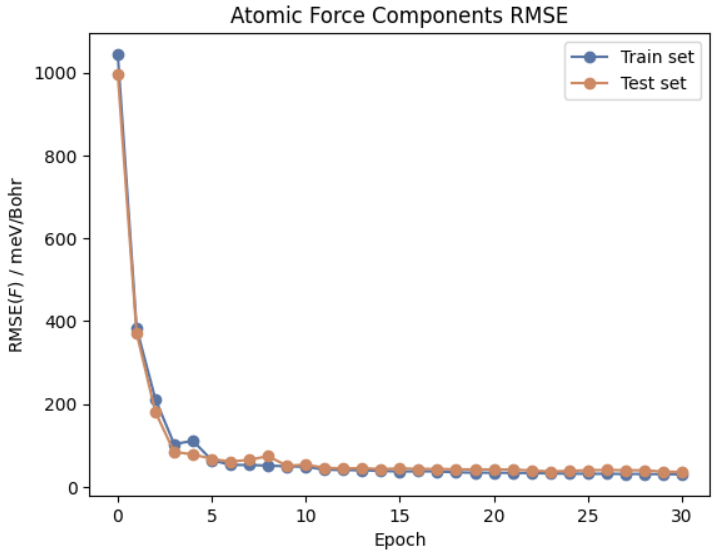

Figure 2.5: Evolution of forces prediction error during the process of training. Forces are calculated from the energy prediction.

14. The energy and force errors obtained from this epoch are provided in Table 2.2.

It is not always the best option to take the weight and biases setup from the last epoch despite it having the smallest error. As was mentioned in Section 1.2.3, errors on the train data will always decrease, however, errors on the test data will at some point start to increase. This point indicates that the model becomes overfitted and loses its ability to predict. Another way how to determine the quality of prediction is to compare data from the data set and the predicted data. In an ideal case, I should

Table 2.2: The error in prediction of energies and forces from epoch 14.

RMSE	train data	test data
Energy [eV/atom]	0.0015	0.0024
Force [eV/Bohr]	0.0382	0.0425

observe equality in the ratio of the predicted energy (model) and the reference energy (DFT) which can be represented with a linear function. The relations between the reference energies and forces and the prediction of the model are shown in Figures 2.6 and 2.7. These types of plots are referred to as correlation graphs. The correlation

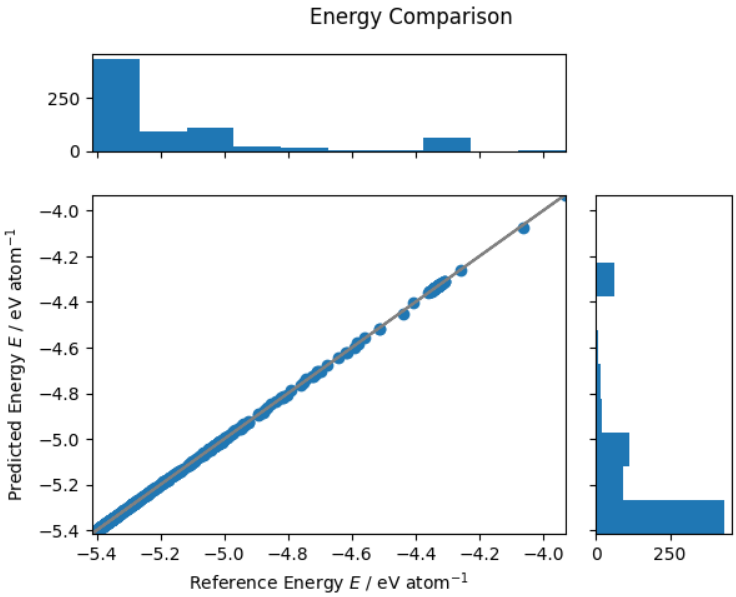

Figure 2.6: The relation between reference energies from DFT calculation and predicted energies. Data are taken across the data set.

graphs show that is NN potential model of silicon follows very well the energies and forces calculated by DFT as well as preserves their distribution, as shown in the histograms in Figures 2.6 and 2.7.

2.1.4 Elastic constants

As a first insight into the physical properties of created interatomic potential, I evaluate the elasticity tensor. To do so, the elasticity tensor is obtained from the relation between energy and strain

$$\Psi(\epsilon) = \frac{1}{2} C_{ijkl} \epsilon_{ij} \epsilon_{kl} \tag{2.6}$$

where Ψ in energy, C_{ijkl} represents elastic constants an ϵ is strain, for more details see Ref. [32]. Using the stress-strain relation from Equation (2.3), elastic constants

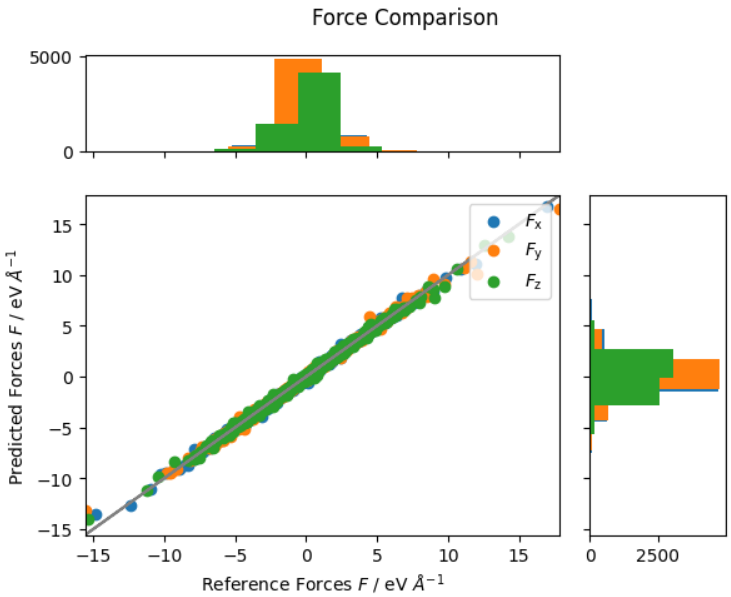

Figure 2.7: The relation between reference forces form DFT calculation and predicted forces. Data are taken across the data set.

can be calculated directly from the energy as

$$\sigma_{ij} = \frac{\partial \Psi}{\partial \epsilon_{ij}} = C_{ijkl}\epsilon_{kl}$$

$$C_{ijkl} = \frac{\partial \Psi}{\partial \epsilon_{ij} \partial \epsilon_{kl}} \tag{2.7}$$

I will use this approach which is implemented in LAMMPS. The calculation is based on static straining of the system during which the change of the energy is extracted at 0 K without entropy effect. The calculated elastic constants with the use NN potential have the following form with values in GPa.

$$\text{NN potential} \Rightarrow \begin{pmatrix} 167.92 & 55.90 & 55.90 & 0 & 0 & 0 \\ 55.90 & 167.92 & 55.90 & 0 & 0 & 0 \\ 55.90 & 55.90 & 167.92 & 0 & 0 & 0 \\ 0 & 0 & 0 & 69.97 & 0 & 0 \\ 0 & 0 & 0 & 0 & 69.97 & 0 \\ 0 & 0 & 0 & 0 & 0 & 69.97 \end{pmatrix} \tag{2.8}$$

It is important to mention that the values of the elastic constant are averaged to two digits and that all elements of the tensor are not exactly zero. To compare the elastic constants from the NN potential with those predicted by DFT, I provide the elasticity tensor obtained from DFT using the same computational setup as was

used for the data set.

$$\text{DFT} \Rightarrow \begin{pmatrix} 159.68 & 63.11 & 63.11 & 0 & 0 & 0 \\ 63.11 & 159.68 & 63.11 & 0 & 0 & 0 \\ 63.11 & 63.11 & 159.68 & 0 & 0 & 0 \\ 0 & 0 & 0 & 76.10 & 0 & 0 \\ 0 & 0 & 0 & 0 & 76.10 & 0 \\ 0 & 0 & 0 & 0 & 0 & 76.10 \end{pmatrix} \tag{2.9}$$

Note that the differences between the elastic constants computed with the NN potential (Equation (2.8)) and by DFT (Equation (2.9)) are small. These differences can have the origin in the small data set and the order of energy prediction error as well as from the slightly different implementation of the employed codes for elasticity tensor calculation. For comparison, I calculate the elastic constants using existing analytical Tersoff potential presented in Ref. [34]. The resulting elasticity tensor is giving in the following matrix (2.10), in GPa units

$$\text{TERSOFF} \Rightarrow \begin{pmatrix} 172.57 & 64.57 & 64.57 & 0 & 0 & 0 \\ 64.57 & 172.57 & 64.57 & 0 & 0 & 0 \\ 64.57 & 64.57 & 172.57 & 0 & 0 & 0 \\ 0 & 0 & 0 & 81.29 & 0 & 0 \\ 0 & 0 & 0 & 0 & 81.29 & 0 \\ 0 & 0 & 0 & 0 & 0 & 81.29 \end{pmatrix} \tag{2.10}$$

According to the calculated elastic constants (2.8) - (2.10) the NN potential for Si succeeds in providing accurate results relative to the DFT values, even though the size of the data set is relatively small. The values are comparable to those obtained by existing potentials based on other methods, DFT, and experimental data within reasonable error. The elasticity tensor predicted by the NN potential shows that the cubic symmetry of the material is preserved, despite such symmetries were not imposed in the creation of the data set.

2.1.5 Phonon dispersion

Another convenient way to analyze the accuracy of potential is through phonon dispersion. Phonon dispersion capture the fundamental properties of the lattice dynamics, especially in low frequencies which correspond to the acoustic phonon band. The negative values of frequencies indicate structural instability. Such knowledge can be very valuable information for the evaluation of the accuracy of the NN potential, thus helping with the improvement of the dataset. The phonon dispersion calculation can be demanding, especially in DFT. A common approach used to obtain the phonon dispersion of a system composed of atoms implies the calculation of the dynamical matrix [36]. To do so, the system is decomposed into primitive cells marked with indexes a. The dynamical matrix is defined by

$$D^{\kappa,\kappa'}_{\alpha,\alpha'}(\mathbf{q}) = \frac{1}{\sqrt{M_\kappa M_{\kappa'}}} \sum_a \frac{\partial^2 E}{\partial \mathbf{u}_{\alpha,\kappa,a} \partial \mathbf{u}_{\alpha',\kappa',a}} e^{-i\mathbf{q}\mathbf{R}_a} \tag{2.11}$$

where **q** is the wave vector, M is mass, κ represents the index of atom in the primitive cell, α represents cartesian coordinates, **u** is the vector of displacement and summation goes over all primitive cells in the system. The eigenvalues of the dynamical matrix correspond to the modes of the strucutre. The effect of the temperature is not included, thus the calculation of the phonon dispersion refers to the ground state at 0 K. Although it is possible to calculate the phonon dispersion at finite temperature by MD simulation, this is out of the scope of this work. Such a methodology is presented in Ref. [36]. I calculated the phonon spectra from the dynamical matrix with the use of LAMMPS and the tool Phonopy [37, 38]. The results were compared to phonon spectra from the theoretical calculation and the experimental measurement. Figure 2.8 the phonon dispersion predicted by the NN potential. The frequencies are in Terahertz. The first important property is that the

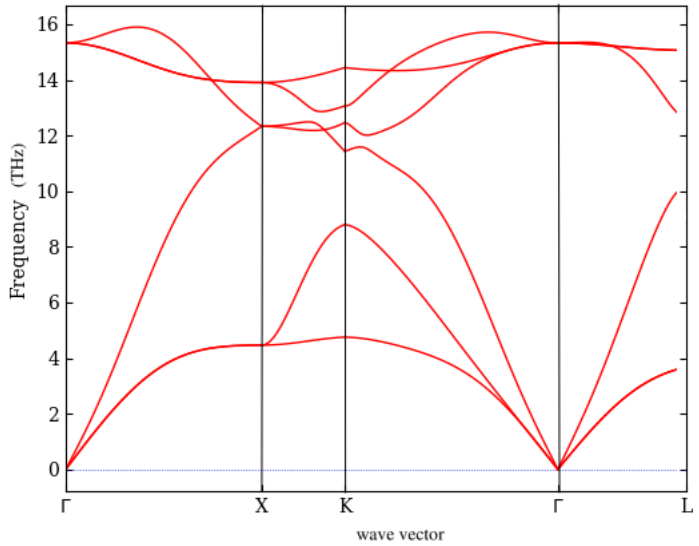

Figure 2.8: The phonon spectra calculated from the dynamical matrix. The y-axis is in THz and the x-axis refers to the wave vectors.

there is no negative branch. The occurrence of a negative branch would point to structural instability of Si ground state in relaxed structure. Figure 2.9 shows the phonon dispersion predicted by theoretical calculation (solid line) and from experimental measurements by neutron diffraction (black points), see Ref. [39]. Comparing the results shown in Figures 2.8 and 2.9, the phonon dispersion calculated by the NN potential is in good agreement with theoretical and experimental results, where both figures show similar frequency ranges (up to 16 THz) and reasonably comparable shapes of the phonon branches.

2.2 Neural network potential for NiTi

In the previous section, I demonstrated that the NN potential approach is suitable to capture the properties of silicon. This section aims to create the potential for NiTi

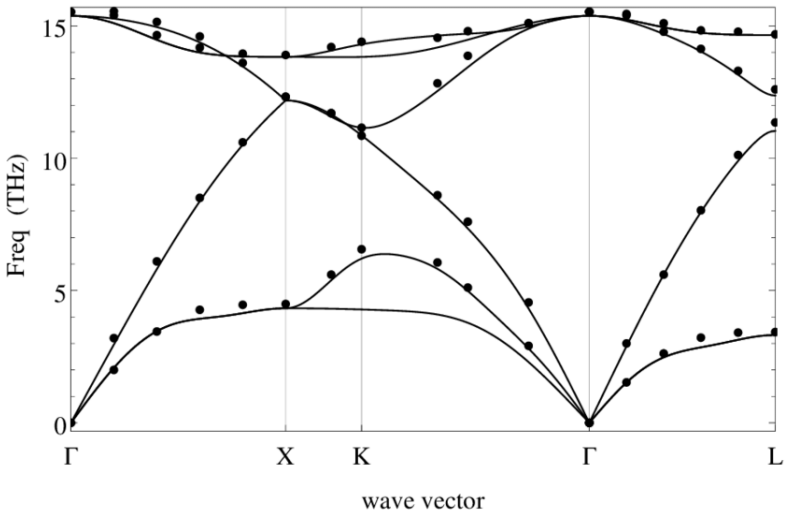

Figure 2.9: The phonon spectra from theoretical calculation (solid line) and experimental measurement (black points). Figure taken from Ref. [39].

in the martensitic phase and investigate basic physical properties such as elastic constants and phonons dispersion. As I am focused on the martensitic phase I will investigate the properties of the B19' and B33 phases. The austenitic phase is out of the scope of this work. The analysis includes, whether the NN potential preserves the shear anisotropy. The results will be compared to reference DFT data or calculation of the semiempirical 2NN-MEAM potential presented in Ref. [40].

2.2.1 Basic properties of NiTi

The martensitic phase of NiTi occurs in the monoclinic B19' structure with the B33 as the theoretical ground state. The lattice vector values are summarized in Table 2.3, parameters for martensitic B19' phase are taken from the experimental measurements presented in Ref. [41, 42]. Interestingly, the DFT calculation consistently results in B33 as a ground state. The lattice parameters of the B33 structure may slightly differ based on the DFT calculation setup. Here, I present the data obtained in Ref. [25] using PAW-LDA potential. The primitive cell of NiTi contains four atoms, two atoms of nickel (Ni) and two atoms of titanium (Ti). The fraction coordinates of the atoms in B19' are summarized in Table 2.4, where the data are taken from the experimental measurement [41, 42]. The values of the atom's fraction coordinates in the B33 phase depend on DFT calculation setup, thus are not listed in this section but will be discussed in the following section. Figure 2.10 shows the primitive cells of B19' and B33. The lattice vectors are expressed in the Cartesian coordinates system 1, 2, 3. The directions of the Cartesian 1- and 2-directions fall in line with a and b lattice vectors.

The determination of the elastic tensor of NiTi martensitic phase is a challenging task, both by experiments and computations. The experimental determination is complicated due to the preparation of a suitable single-variant sample. The theoretical calculation has difficulties with the tendency to converge into B33 through

Table 2.3: The lattice parameters of the monoclinic B19' and B33 structure. The data taken from experimental measurement presented in Ref. [41, 42]. Data for the B33 structure are taken from theoretical calculations presented in Ref. [25].

	a(Å)	b(Å)	c(Å)	β(deg)
B19' [41]	4.646	4.108	2.898	97.78
B33 [25]	4.815	3.921	2.851	107.2

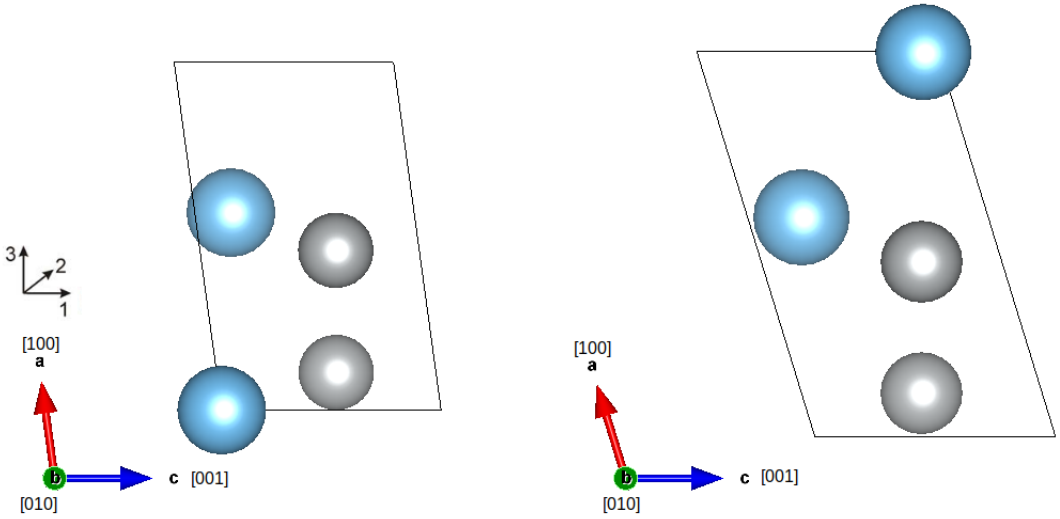

(a) B19' (b) B33

Figure 2.10: The primitive cell of (a) B19' and (b) B33. For B19'; lattice vectors and fraction coordinates are taken from Table 2.3 and 2.4. For B33, lattice vectors and fraction coordinates are taken from minimization with here resented setup. The lattice vectors are expressed in the Cartesian coordinates system 1, 2, 3. The directions of the Cartesian 1- and 2-directions fall in line with c and b.

Table 2.4: The fraction coordinates of atoms in B19' unit cell. The data taken from Ref. [41, 42].

	x	y	z
Ti_1	0	0	0
Ti_2	0.5672	0.5	0.1648
Ni_1	0.4588	0.0	0.6196
Ni_2	0.1084	0.5	0.5452

minimization. Moreover, B19' is a monoclinic structure, thus it has 13 independent elastic constants. The DFT calculation of the elastic tensor is presented in Ref. [43]

and predicts the following elasticity tensor (all values are in GPa)

$$\text{B19'} \Rightarrow \begin{pmatrix} 209 & 114 & 102 & 0 & 1 & 0 \\ 114 & 234 & 139 & 0 & -7 & 0 \\ 102 & 139 & 238 & 0 & 27 & 0 \\ 0 & 0 & 0 & 77 & 0 & -5 \\ 1 & -7 & 27 & 0 & 23 & 0 \\ 0 & 0 & 0 & -5 & 0 & 72 \end{pmatrix} \tag{2.12}$$

The elasticity tensor for B33 primitive cell was calculated using DFT in Ref. [44]

$$\text{B33} \Rightarrow \begin{pmatrix} 247 & 137 & 113 & 0 & 33 & 0 \\ 137 & 231 & 134 & 0 & 1 & 0 \\ 113 & 134 & 179 & 0 & -18 & 0 \\ 0 & 0 & 0 & 84 & 0 & 2 \\ 33 & 1 & -18 & 0 & 23 & 0 \\ 0 & 0 & 0 & 2 & 0 & 90 \end{pmatrix} \tag{2.13}$$

A more detailed comparison of the calculation of the elasticity tensor can be found in Ref. [41, 44].

The experimental values of phonon dispersion are not available, the theoretical study of the phonon dispersion was published in Ref. [45], the results for B19' and B33 are shown in Figure 2.11.

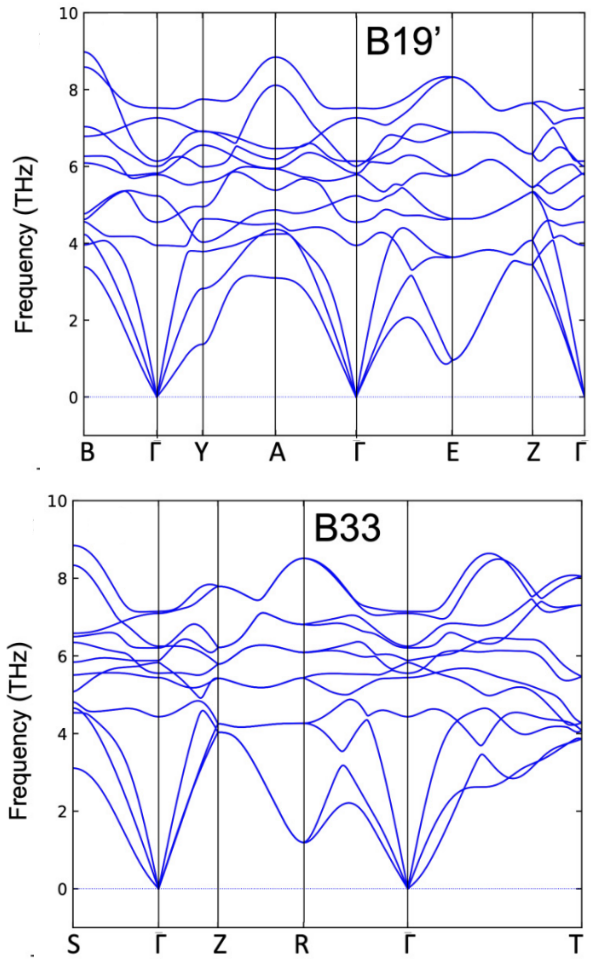

Figure 2.11: The phonon spectra of B19' and B33. The data are calculated with the use of DFT. Figure taken from Ref. [45].

2.2.2 The data set for neural network potential

The data set contains 200 structures of a mixture of larger cells which are two and three times larger in each direction than primitive cells (2x2x2 and 3x3x3 superlattices) and primitive cells which are sampled around the transition path between B19' and B33. The structures in the data set are added iteratively. The first part of the data set represents the random fluctuations. Then the structures obtained from MD (with use of the newly created NN potential) at different temperature levels are added. In the data set are also structures that are compressed to 97 % of their original volume and the random displacement of the magnitude of 0.2 Å is applied. The random displacement of the magnitude of 0.2 was also applied to the structures without compression. In the data set are included the shearing structures of B19' in (100)[001] direction.

In total, the data set contains around 200 structures, this number could seem small, on the other hand, the structures contain more atoms, in the total data set contains around 6600 atom configurations.

Energies and forces are calculated with the use of VASP. The Brillouin zone was

sampled with a Monkhorst-Pack net with 24 k-points in each direction of reciprocal lattice vectors for calculation on primitive cells. The number of points was adjusted depending on the size of the structure, for x-times larger cell was used x-times smaller sampling. It is important to note that such sampling is anisotropic. The lattice vectors of B19' therefore the vectors of reciprocal space do not have the same length, thus some directions of reciprocal space would be more sampled than others. These inhomogeneities can cause errors in the forces calculations on the other hand they allow us to calculate the same k-points independently of the size of the structure. The calculation in the same k-point is for the anisotropic materials such as NiTi much more important, thus I decided to use the same number of points in each direction. The influence of sampling on the calculation of the forces and the error was below 0.000395 eV/Å which is neglectable for our purpose.

The size of the plane-wave basis was set to 650 eV. The PAW potential with the PBE exchange-correlation function is used for both elements. Due to the random fluctuation, no symmetries could be used for the speed-up of the calculations. For Ni, potential with valency 10, and for Ti, potential with p-valence electrons with valency 10 (further denoted as Ti-pv).

B19'

The dependency of energy per atom on the plane-wave basis is shown in Figure 2.12, values of the energies are in Table 2.5. The values in Table 2.5 show, that from the 600 eV plane-wave basis size the values of the energies per atom have convergence in order of 0.1 meV/atom which is more than sufficient for the data set.

The dependence on the sampling in the Brillouin zone is shown in Figure 2.13. All values are within the error in order of 0.1 meV/atom. I decided to use 24 k-points for the sampling in each direction of the reciprocal lattice because 24 is divisible by 2,3 and 4. This is important for the computation of the superlattices 2x2x2 and 3x3x3, where I need to adjust the number of k-points .

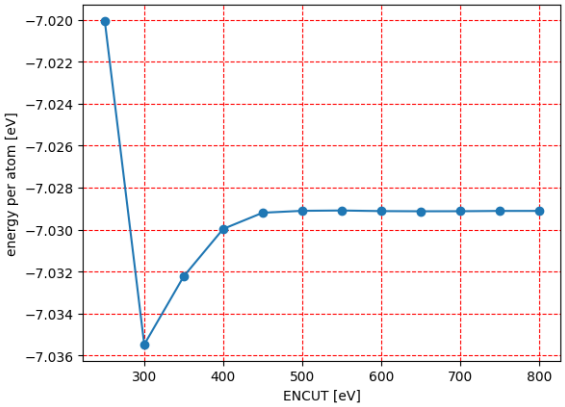

Figure 2.12: Relation between the energy per atom and size of the plane-wave basis marked as ENCUT.

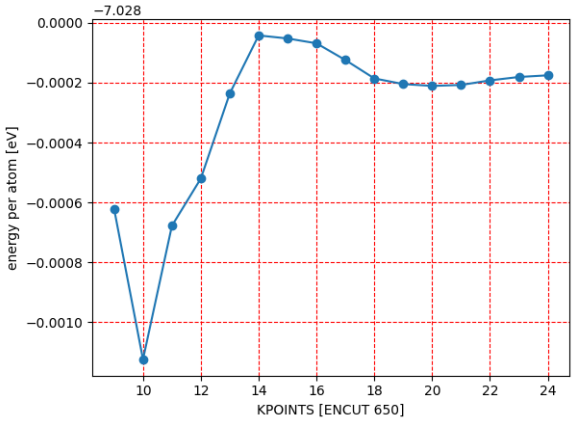

Figure 2.13: The relation between sampling of the Brillouin zone and calculated energy per atom. The number on the x-axis represents the number of points used in sampling in each direction of the reciprocal lattice vectors.

Table 2.5: Dependence of calculated energy per atom of B19' phase on size of the plane-wave basis.

plane-wave basis [eV]	energy [eV]	plane-wave basis [eV]	energy [eV]
250	-7.02006342	550	-7.02908775
300	-7.03546932	600	-7.02911627
350	-7.03222247	650	-7.02912461
400	-7.02996445	700	-7.02912202
450	-7.02919416	750	-7.02910879
500	-7.02910310	800	-7.02910738

B33

The B33 structure was obtained by minimizing B19' with the use of the conjugate gradient method implemented in VASP. The plane-wave basis size was set to 650 eV, and the reciprocal space was sampled using a Monkhorst-Pack net with 15 k-points in each direction of reciprocal lattice vectors. Both Ni and Ti were modeled using the PAW-PBE potential, for Ti a potential with p-valence electrons was used. The reason why I used smaller sampling in reciprocal space will be discussed in the following section. The parameters obtained from the minimization are written in Table 2.6. Figure 2.14 shows the conventional cell suggested by red rectangular. The conventional cell reflects the orthorhombic symmetries. The orthorhombic B33 conventional cell can be obtained by rotation along the 2-axis of the Cartesian coordinates system, such a rotation orients the 1'- and 3'-direction parallel to the orthorhombic lattice. The atom position in the B33 structure from the minimization is expressed in Table 2.7 in fraction coordinates. The lattice parameters are comparable with results presented in literature Ref. [25].

To ensure that my calculation setup is also suitable for the B33 structure I calculated the energy dependencies on a plane-wave basis and k-points sampling as I did for

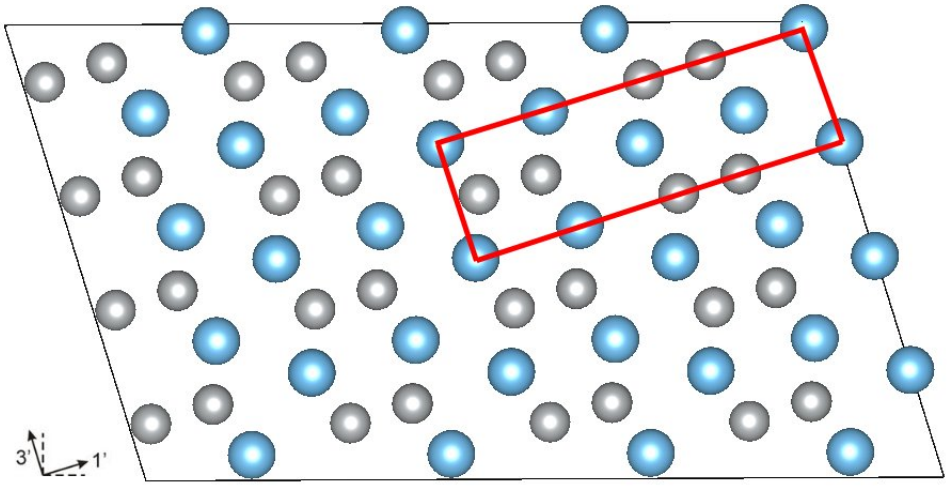

Figure 2.14: The orthorombic cell of the B33 mark by the solid red line.

Table 2.6: The lattice parameters obtained after minimization from B19' structure. All parameters, such as lattice parameters, angles, and atom positions had a degree of freedom.

	a(Å)	b(Å)	c(Å)	$\alpha(deg)$	$\beta(deg)$	$\gamma(deg)$
B33	4.90806	4.00592	2.92304	90.00	107.01	90.00
B33 [25]	4.815	3.921	2.851	90.00	107.20	90.00

Table 2.7: The fraction coordinates of atoms in B33 structure observed through minimization.

	x	y	z
Ti_1	-0.00246	0.00	-0.05935
Ti_2	-0.56966	0.50	0.22415
Ni_1	0.11233	0.50	0.49775
Ni_2	0.45487	0.00	0.66705

B19' structure. In Figures 2.15 and 2.16 are plotted energy differences per atom B19' - B33. The error in plane-wave basis energies is on the order of 0.01 meV/atom and for the k-points sampling is on the order of 0.1 meV/atom, for the same setting as was used for B19'. Thus the quality of the NN potential fit is limited by the error of the order of 0.1 meV/atom.

Note to the minimization

In this section, it was previously stated that 24 k-points would be used in each direction of reciprocal lattice vectors for all calculations, or the number would be adjusted based on the size of the superlattice to preserve the same density of k-

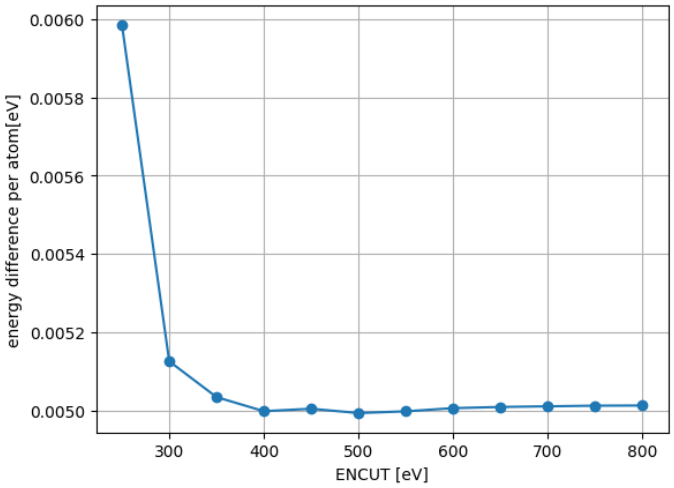

Figure 2.15: The energy difference between B19' and B33 depended on the size of plane-wave basis.

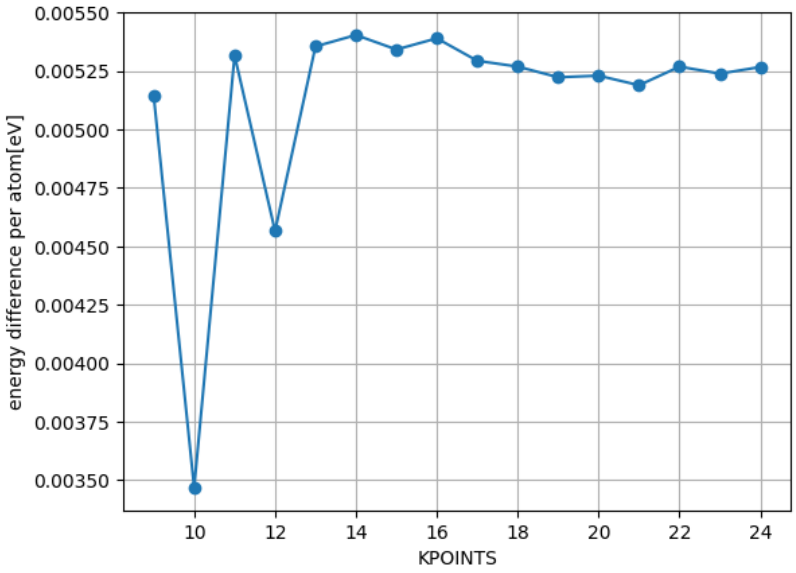

Figure 2.16: The energy difference between B19' and B33 depended on the number of k-points in reciprocal space. The number on the y-axis represents the number of points used in each direction of the reciprocal space basis vectors. The plane-wave basis was set to 650 eV.

points. However, during the minimization process, only 15 k-points were used in each direction of reciprocal lattice vectors. The reason behind this change is that I was not able to capture the ground state B33 structure with the use of 24 k-points. Finer sampling in the Brillouin zone causes the existence of very shallow minima around angle $\beta = 101°$ in step 25, which stops the minimization algorithm. This stop is marked in Figure 2.17 by the red dashed line.

Figure 2.17 shows the calculated energies for the structures from the minimization path of B19' obtained from the minimization with 15 k-points setup. Both calculations have a similar setup but only differ in the density of the reciprocal space

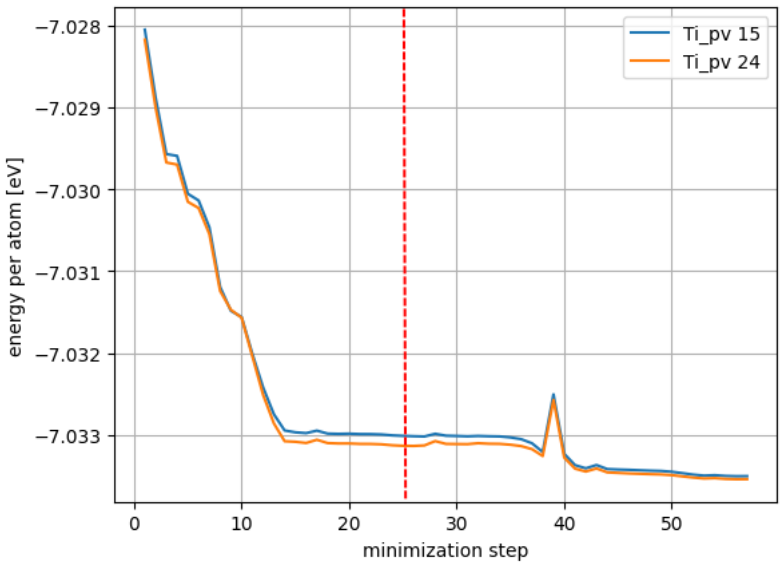

Figure 2.17: The energy evolution during the minimization from B19' to B33. The energy of the whole structure in each minimization step is plotted. The red dashed line suggests the point where the minimization stops for the 24 k-point sampling.

sampling. For both samplings, the B33 is energetically favorable over other structures. The local minimum in step 25 is insignificantly small. Thus, in the data set are used structures from the minimization path with 15 k-points sampling but the energies of these structures are recalculated with the 24 k-points sampling.

2.2.3 Neural network potential

The potential was fitted by the RuNNer code. For the atomic environment description were used atom-centered symmetry function, as was presented in the Theoretical part, see equation (1.25) and (1.27) for radial respectively angular symmetry function. In total 73 radial and angular symmetry functions for each element were used. The radius of the cut-off sphere was set to 6.36 Å and the cut-off function was identical to the equation (1.3.2). The neural network consists of two hidden layers, each containing 15 neurons; hyperbolic tangent was used as an activation function, and in the output layer was used linear activation function. The test dataset was 10% of the whole dataset and during the learning 10% of forces were used. I used 30 epochs to train the neural network. A detailed description of all symmetry functions and the setup is in the Attachment of this work. As a training algorithm was used Kalman filter was and the cost function was root mean squared error (RMSE)

In Figure 2.18 is presented the energy distribution in the data set. The lowest energies correspond to the B33 structure and the highest energies denote the B19' structures and B19' and B33 structures which were pressed to 97 % and 98 % of their original volume. The lowest energies with the highest count in Figure 2.18 refer to the minimization path from B19' to B33.

In Figure 2.19 and 2.20 is plotted the evolution of the error in the prediction of ener-

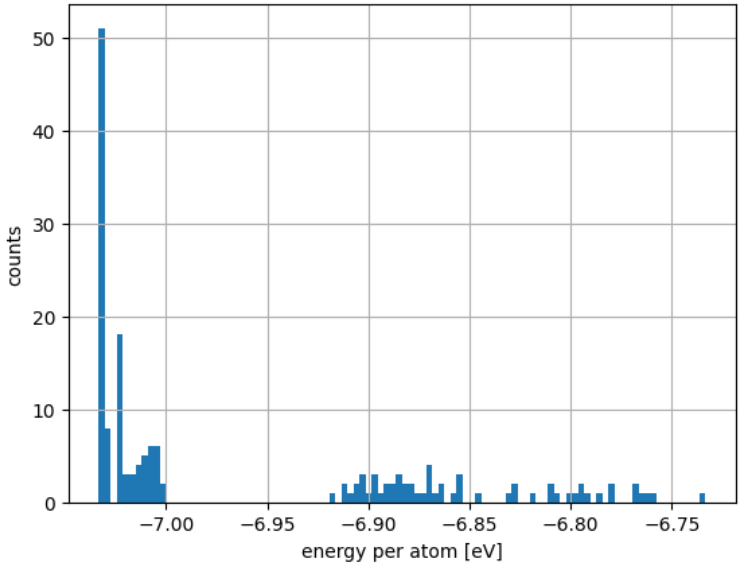

Figure 2.18: Distribution of energy per atom in the whole dataset.

gies and forces respectively. Both errors smoothly converge and the best prediction

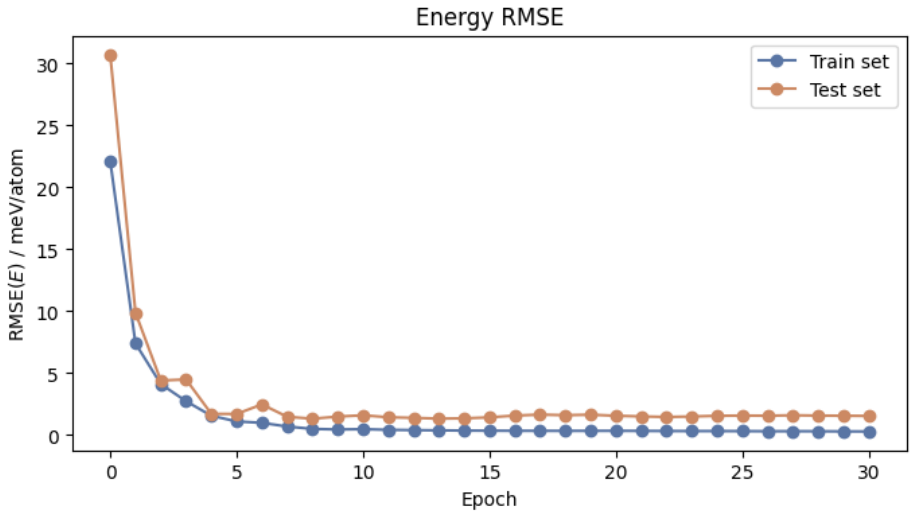

Figure 2.19: The evolution of the energy prediction error during the process of training. The energy prediction error is per atom.

was observed in epoch 8. In the following section I will used the weight and biases from this epoch. These errors are written in Table 2.8. The fit reached an accurate prediction in the energy, all errors are within the range of DFT calculation accuracy. The Figures 2.21 and 2.22 show the correlation graphs for the energy and forces, respectively.

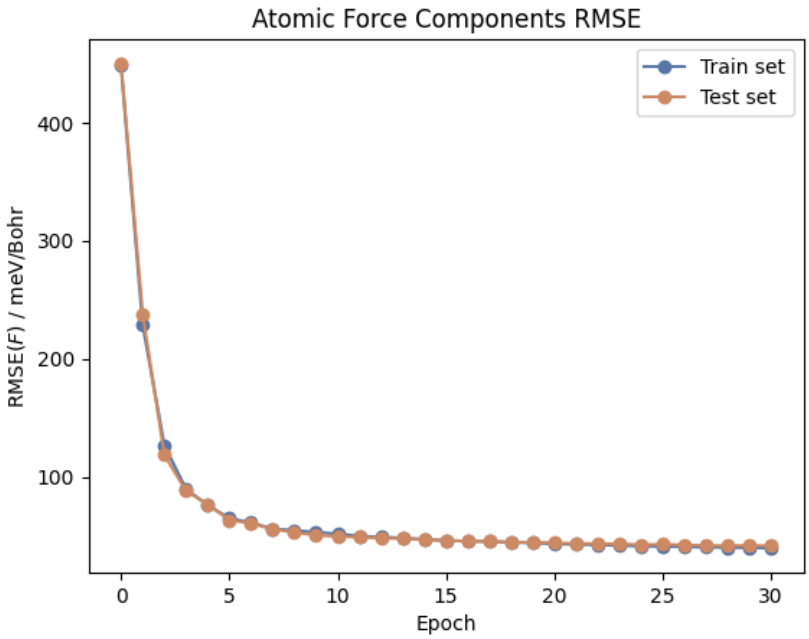

Figure 2.20: The evolution of the forces prediction error during the process of training. Forces are calculated from the NN potential energy prediction. The forces prediction error is per atom.

Table 2.8: The error in prediction of energies and forces from epoch 8.

RMSE	train data	test data
Energy [eV/atom]	0.0005	0.0013
Force [eV/Bohr]	0.0546	0.0529

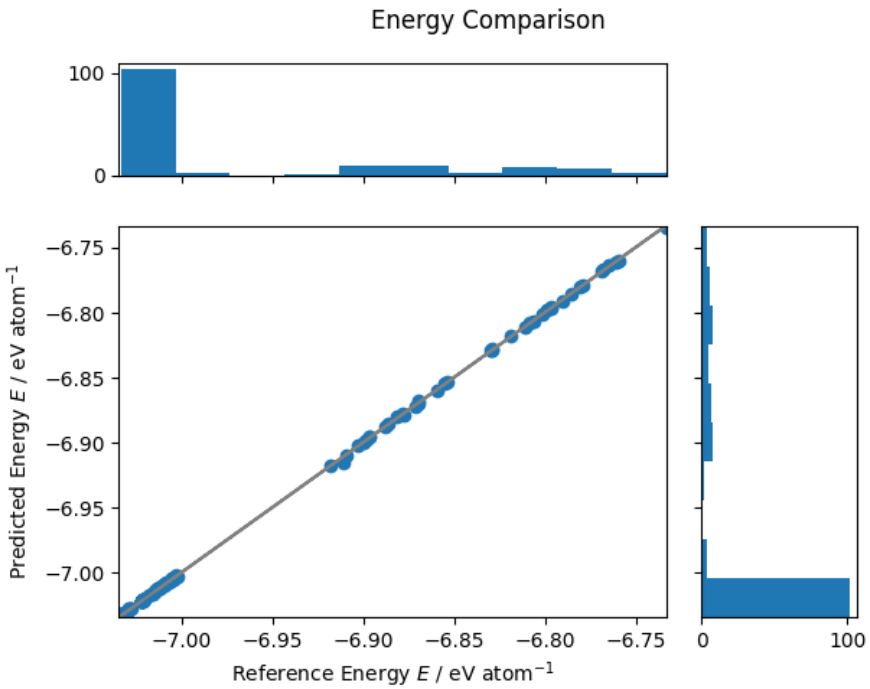

Figure 2.21: The relation between reference energies from DFT calculation and predicted energies. Data are taken from the all structures in the data set

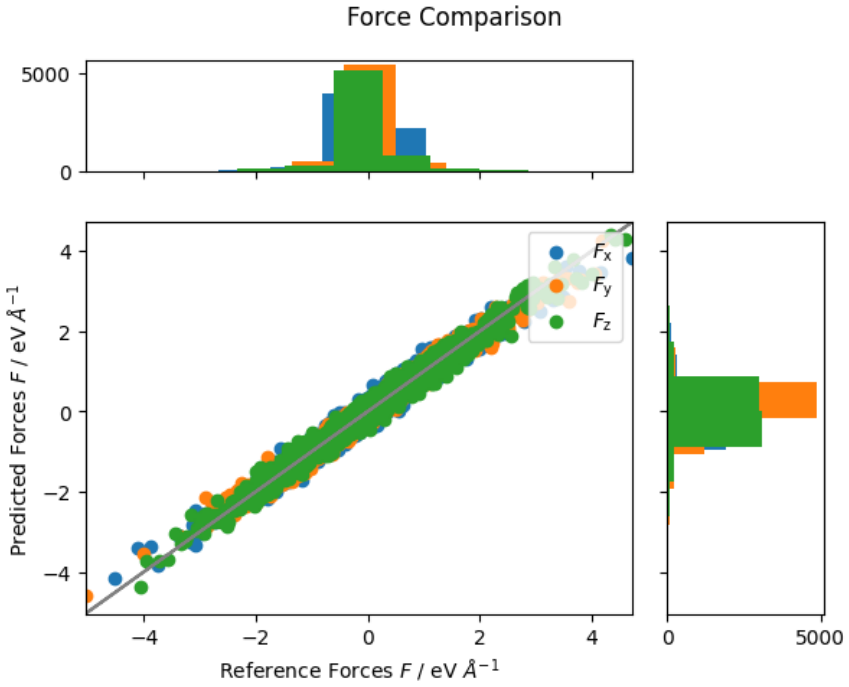

Figure 2.22: The relation between reference forces form DFT calculation and predicted forces. Data are taken from all structures in the data set

2.2.4 Elastic constants

The calculation is based on static straining of the system and observing the change of the energy, thus all data are calculated at 0 K without entropy effect, it is the same methodology that was used for Si potential.

B19'

The calculated elasticity tensor with NN potential has the following form, all values are in GPa and averaged to two digits

$$\text{NN potential} \Rightarrow \begin{pmatrix} 332.23 & 167.35 & 226.39 & 0 & -7.82 & 0 \\ 167.35 & 245.72 & 123.62 & 0 & -48.34 & 0 \\ 226.39 & 123.62 & 210.51 & 0 & -22.34 & 0 \\ 0 & 0 & 0 & 87.62 & 0 & -4.86 \\ -7.82 & -48.34 & -22.34 & 0 & 23.11 & 0 \\ 0 & 0 & 0 & -4.86 & 0 & 48.69 \end{pmatrix} \tag{2.14}$$

The calculated elasticity tensor preserved the monoclinic symmetry and is comparable with the values presented in the literature. The biggest differences to the data from the literature are in C_{15}, C_{25} and C_{35} elastic constants. This direction can be the subject of further development. For the comparison, the elasticity tensor was calculated with the same structure and methodology using the 2NN-MEAM potential presented in Ref. [40]. The values are in good agreement with the DFT calculation, see Table 2.9.

B33

I calculated the elasticity tensor for both, the monoclinic primitive cell of B33 and for the orthorhombic conventional cell. The elasticity tensor for the orthorhombic cell was obtained by rotation of the coordinates system around 2-axis, see Figure 2.14. The NN potential preserves sufficiently the orthorhombic symmetry. The calculated elasticity tensor orthorhombic cell with NN potential has the following form, all values are in GPa and averaged to two digits.

$$\text{NN potential} \Rightarrow \begin{pmatrix} 430.19 & 235.42 & 278.33 & 0 & 9.34 & 0 \\ 235.42 & 337.34 & 197.32 & 0 & -1.73 & 0 \\ 278.33 & 197.32 & 99.54 & 0 & -3.30 & 0 \\ 0 & 0 & 0 & 90.55 & 0 & 0.04 \\ 9.34 & -1.73 & -3.300 & 0 & 23.11 & 0 \\ 0 & 0 & 0 & 0.04 & 0 & 56.12 \end{pmatrix} \tag{2.15}$$

There is no available interatomic potential for B33, thus I can only compare the values of the elastic constants with the results from DFT calculation, provided in Equation (2.13).

Table 2.9: Values of elastic constants of B19' phase. The values of elastic constants computed by NN potential are compared to values obtained by DFT in Ref. [44] and to the values predicted by the 2NN-MEAM potential in Ref. [40].

	DFT [GPa] [44]	NN potential [GPa]	2NN-MEAM [GPa] [40]
C_{11}	226	332.23	197.04
C_{22}	241	245.72	227.72
C_{33}	179	210.51	186.86
C_{12}	137	167.35	100.87
C_{13}	129	226.39	80.54
C_{15}	27	-7.82	12.44
C_{23}	125	123.62	117.10
C_{25}	-9	-48.34	-12.31
C_{35}	4	-22.34	1.12
C_{44}	76	87.62	66.43
C_{46}	-4	-4.86	-8.22
C_{55}	21	23.11	57.23
C_{66}	77	48.69	40.42

Table 2.10: Values of elastic constants of B33 phase in the coordinate system shown in Figure 2.10 and in the principal orthogonal directions in Figure 2.14 (denoted as "ortho."). The values of NN potential are compared to values obtained by DFT calculation in Ref. [44].

	DFT [GPa] [44]	DFT - ortho. [GPa] [44]	NN [GPa]	NN - ortho. [GPa]
C_{11}	226	247	406.70	430.19
C_{22}	231	231	337.34	337.34
C_{33}	179	179	132.0	99.54
C_{12}	137	137	235.42	237.70
C_{13}	113	96	278.33	195.03
C_{15}	33	-5	32.55	9.34
C_{23}	134	134	197.32	282.82
C_{25}	1	0	9.77	-1.73
C_{35}	-18	2	59.67	-3.30
C_{44}	84	83	87.99	90.55
C_{46}	2	0	-0.03	0.04
C_{55}	23	23	23.11	27.60
C_{66}	90	90	58.68	56.12

2.2.5 Phonon dispersion

I calculated the phonon dispersion with the use of LAMMPS and the tool Phonopy. The calculations are static and were held at 0 K. The calculated phonon dispersion curve from Figure 2.23 have similar shapes of branches as the published one in Figure 2.11. Both structures have a similar range of phonon frequencies and there is no occurrence of negative phonon spectra branches.

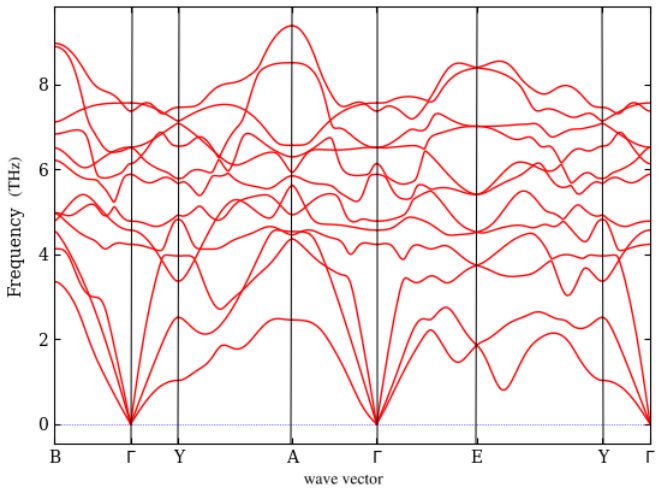

(a) B19'

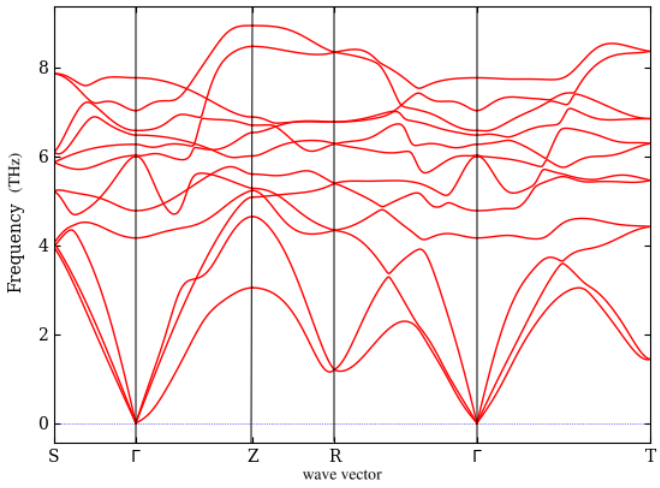

(b) B33

Figure 2.23: The phonon spectra of B19'(a) and B33 (b). The values of the frequencies are in Thz.

2.2.6 Stacking fault energy

The stacking fault energy (SFE), a measure of the energy cost when two adjacent atomic planes are sheared relative to each other, is a critical parameter in plastic deformation [46]. The topology of such an energy landscape can provide us insightful information into the mechanisms for dislocation slip, partial dislocation, or creation of stacking faults in the crystal. The SFE is determined by a difference between a sheared structure and an unperturbed system normalized by the surface between adjacent atomic planes.

$$\gamma = \frac{E_{shear} - E_0}{A} \tag{2.16}$$

where E_{shear} is the energy of sheared system, E_0 is energy of the unperturbed system and A is the surface between adjacent atomic planes.

I examine the SFE surface of the NiTi B19' phase containing 4 primitive cells in [100], [010], [001] directions (further denoted as 4x4x4 structure). The shear would be applied in the (100)[001], (100)[010], (010)[100] directions, and for the (100) plane by shearing in [010] and [001] directions. The energy calculation will be done by NN potential in the program LAMMPS using periodic boundary conditions in all directions. Figure 2.24 shows NiTi 4x4x4 supercell of B19' phase. In Figure 2.24, the red parallelogram denotes the shearing on the (001) plane, the green parallelogram marks the shearing on the (100) plane. The rest of the structure is static. With the application of shearing, the instantaneous SFE is calculated for every configuration. TIn the following section, the resulting SFE profiles obtained from the shearing simulations using the NN potential will be compared to those using the 2NN-MEAM potential from Ref. [40].

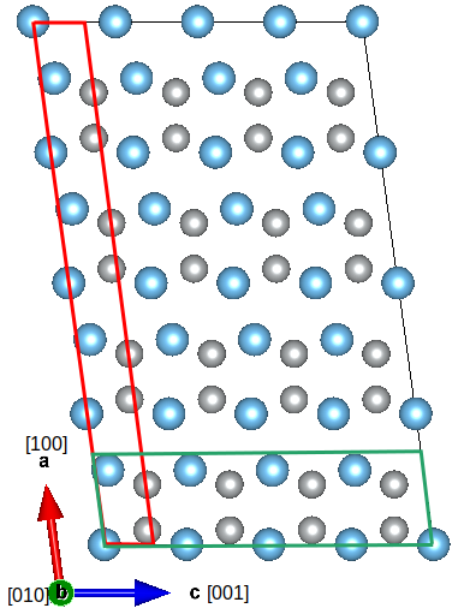

Figure 2.24: Schematics of the applied shearing in B19' NiTi. The red parallelogram area marks shearing on the (001) plane whereas the green green parallelogram denotes shearing on (100) plane.

2.2.7 Shearing responses of B19': NN vs. 2NN-MEAM potentials

Figure 2.25 shows the calculated SFE based on the Equation (2.16) using NN potential. The energies in Figure 2.25 are calculated without minimization. The calculations were made in the (100)[001], (100)[010], (010)[100] directions with shearing step 0.01 Å. In the simulations, the way that the shearing along the slip plane is

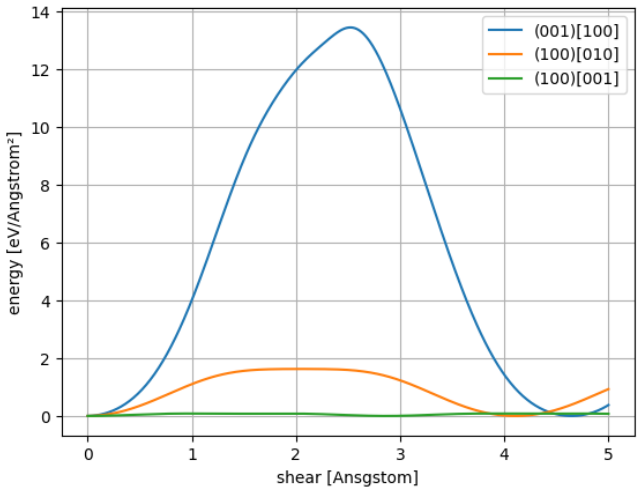

Figure 2.25: SFE in the (100)[001], (100)[010], (010)[100] directions. The energies are obtained without minimization by NN potential. The shearing step is 0.01 Å.

forced leads to atomic environments where atoms are too close to each other that are not included in the dataset. Therefore, the resulting energies and forces are not trustworthy, as shown by the number of extrapolations generated during the simulations in Figure 2.26. In these cases, the results should be taken with great care. The

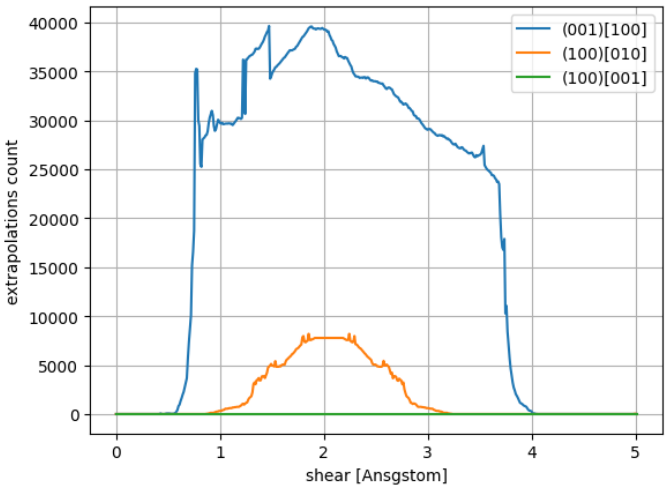

Figure 2.26: The number of extrapolations generated by the NN potential during the simulation of shearing.

number of extrapolations generated by NN potential during the SFE calculation is plotted in Figure 2.26.

From Figures 2.25 and 2.26 is seen that the NN potential reproduces experimentally observed anisotropy of the NiTi B19' phase. The shear in direction (100)[001] is energetically favorable over the other directions which is in agreement with the experiments. Moreover, NN potential model does not generate any extrapolation in this direction. By way of comparison, I run an identical shearing process using the 2NN-MEAM. The results are in Figure 2.27. Confronting the results from newly

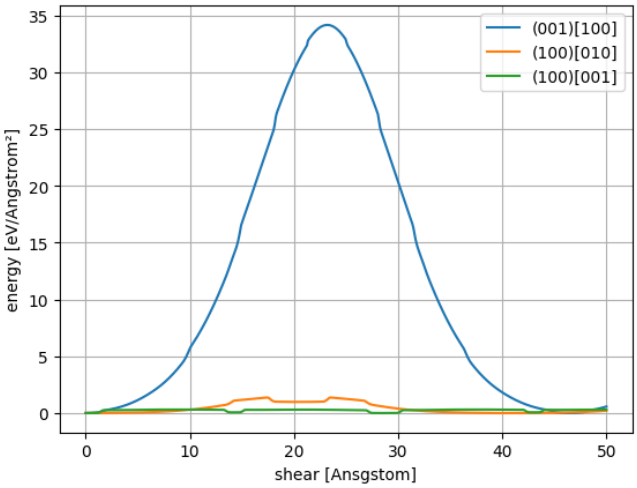

Figure 2.27: SFE in the (100)[001], (100)[010], (010)[100] directions. The energies are obtained without minimization with the use of 2NN-MEAM potential. The shearing step is 0.01 Å.

developed NN potential in Figure 2.25 and from 2NN-MEAM potential in Figure 2.27, it is clear that NN potential preserves the shearing anisotropy. Moreover, the NN potential predicts smoother energy profiles than those predicted by the 2NN-MEAM, compare Figures 2.25 and 2.27. To support such a claim, I will focus more on the energy landscape in (100)[001] direction.

(100)[001]

Because the developed NN generates no extrapolation in (100)[001] direction, I can compare it to the 2NN-MEAM potential. This shear direction has the lowest SFE also during the shear process, the high symmetry orthogonal phase B33 should locally occur, see the Theory part, Figure 1.14.

Figure 2.28 shows the SFE calculated using NN potential. The system reaches the local minimum by shearing by 1.5 Å . Such a minimum is in agreement with the theoretical occurrence of the local high symmetry phase. In Figure 2.29, the SFE computed by 2NN-MEAM potential is plotted. By comparing the Figures 2.28 and 2.29 it is clear that the NN potential outperforms the 2NN-MEAM potential when it comes to energy prediction. The NN potential energy landscape is much smoother. Although both potentials predict a local minimum around the shearing direction (100)[001] at 1.5 Å, the energy landscape obtained by the NN potential is smoother and more well-defined than that predicted by the 2NN-MEAM potential.The height

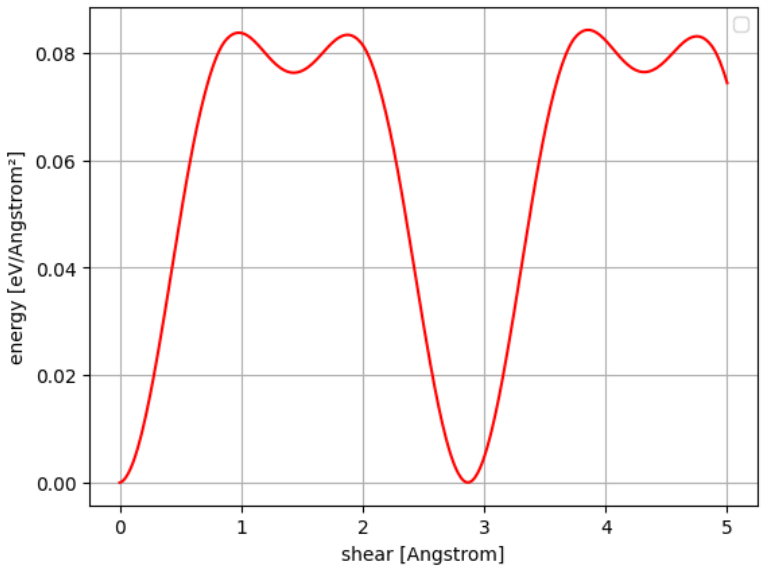

Figure 2.28: SFE during shearing in (100)[001] direction. Energy is calculated by NN potential.

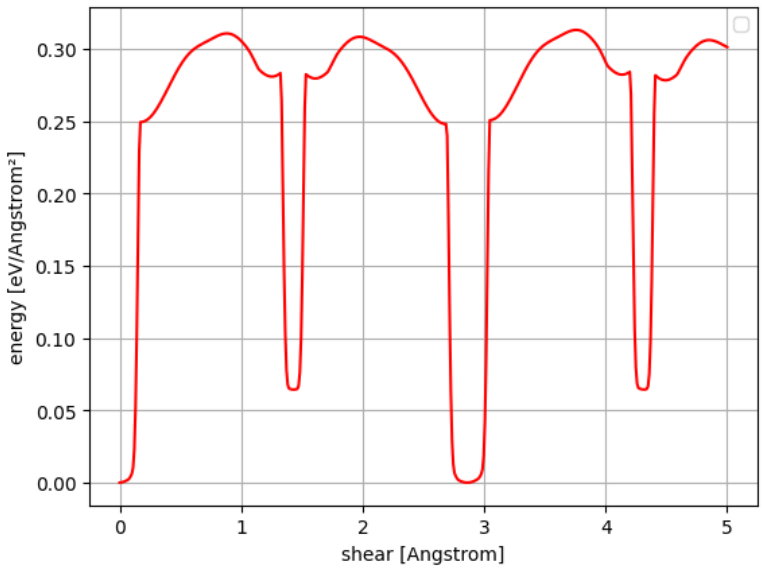

Figure 2.29: SFE during shearing in (100)[001] direction. Energy is calculated by 2NN-MEAM potential.

of the energetic barrier differs by the order. This can be caused by the use of a different DFT setup in the calculation of the data set.

2.2.8 Possible slip pathways on the (100) slip plane

In this chapter, a more detailed study of SFE will be presented. I will examine the SFE values on the (100) plane by shearing the red parallelogram as is shown in Figure 2.24 in [010] and [001] directions. The shearing magnitude is 0.1 Å and

periodic boundary conditions were used in all directions. The energies are calculated by the NN potential.

This plane exhibits high anisotropy. The easy shear in (100)[001] direction and the occurrence of the high energetic barrier in the area of shear at 2 Å in the (100)[010] direction. The existence of such a barrier causes the easy shear only in the (100)[001] direction This is in good agreement with the experiments. Moreover, the topology of SFE on the (100) plane suggests the existence of a saddle point and a possible slip pathway. Such a path is marked by red arrows in Figure 2.30

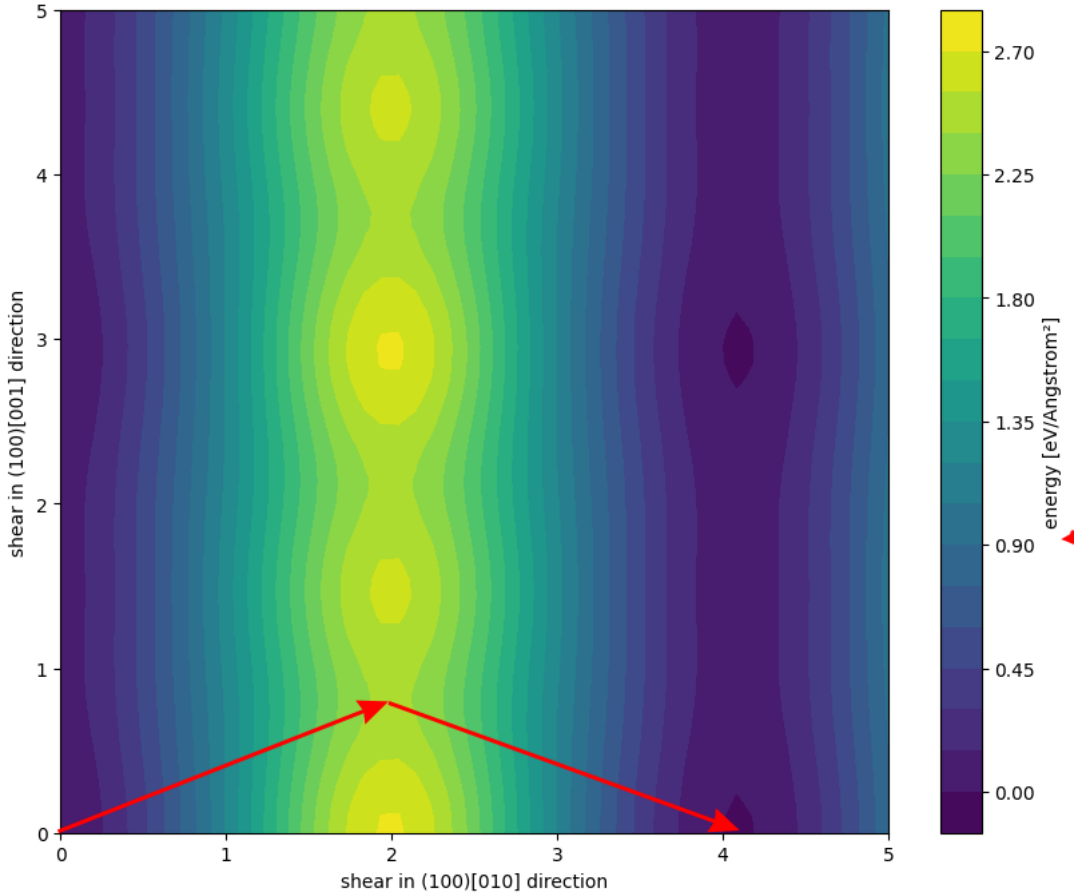

Figure 2.30: SFE in the (100) plane. The energies are calculated by the NN potential. Red arrows mark the possible slip pathway.

Figure 2.31 shows the extrapolations generated by the NN potential during shearing in the (100) plane, where the largest number of extrapolations coincide with the structures representing situations when the atoms are too close to each other. Such structures are not included in the data set.

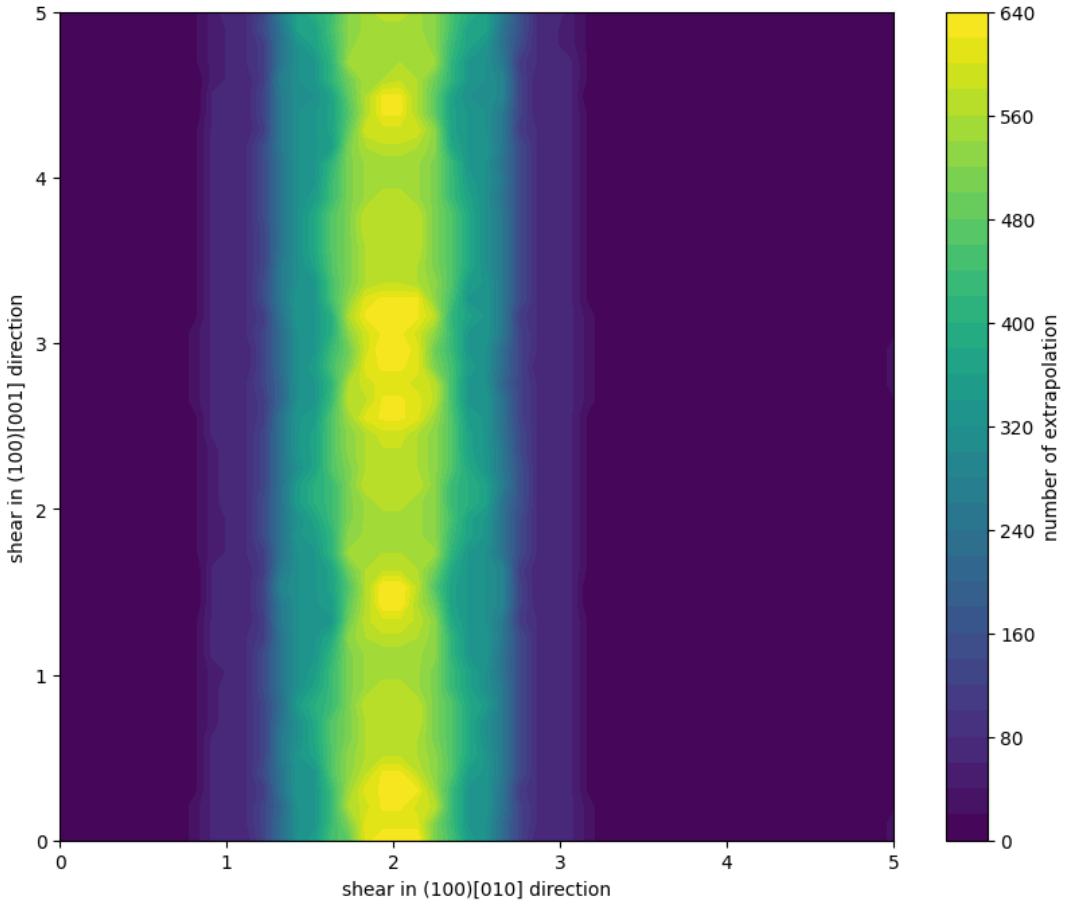

Figure 2.31: The number of extrapolations of the NN potential model during the simulation of the SFE landscape on the (100) plane.

Conclusions

In this work, I present the state-of-the-art methodology for the development of data-driven interatomic potentials using neural networks (NN), involving the generation of an extensive dataset employing density functional theory (DFT) computations. I create the interatomic potential for B19' martensitic nickel-titanium (NiTi) crystals with a focus on the plastic deformation mechanisms and the microstructure evolution.

Overall, this technique allows for the development of accurate potentials for molecular statics (MS) and molecular dynamics (MD) simulations that show accuracy levels comparable to those from ab-inition molecular dynamics DFT calculation. To support this claim, I develop two NN potentials for diamond crystal silicon (Si) and B19' NiTi. To evaluate the accuracy of these NN potentials, I calculate the resulting elastic constants and phonon dispersion curves. Then, I compare these results with those predicted by DFT and those measured in previous experiments. The analysis shows that the NN potentials for both Si and B19' NiTi are fully comparable or outperform the existing parametrized, analytical models (Tersoff for Si, and 2NN-MEAM for NiTi).

This work aimed to develop the NN potential for NiTi B19' martensitic phase. For analytical potential, such a system is a challenging task because these models struggle to capture its complexity. I focused mainly on the elastic properties of the martensitic B19' phase. I use the NN potential for NiTi to assess the energetically favorable plastic slip pathways in the martensitic B19' phase. Such mechanisms remain to be established in the available literature. According to the predictions by the NN potential, the B19' crystal exhibits strong shearing anisotropy, especially in the (100)[001] direction. Under shearing along this direction, the NN potential predicts the existence of a possible saddle point in the stacking fault energy surface on the (100) slip plane, suggesting a possible slip pathway in B19' NiTi.

According to the computational results, the developed NN potential appears to be suitable for MS and MD simulations of B19' NiTi crystals. Nevertheless, the simulations running the current NN potential generate a relatively large number of extrapolations in energy prediction. The dataset presents gaps in the energy distribution, which may cause a loss of generality. The elimination of such faults will be the subject of further research. With the generation of a much richer dataset, the NN potential for NiTi may bring a fundamental insight into the governing plastic mechanisms in B19' martensites.

Literature

1. Seiner, H., Sedlák, P., Frost, M. & Šittner, P. Kwinking as the plastic forming mechanism of B19 NiTi martensite. *International Journal of Plasticity* **168,** 103697. (2023) (Sept. 2023).
2. Tuckerman, M. E. *Statistical Mechanics : Theory and Molecular Simulation* `https://ebookcentral.proquest.com` (Oxford: Oxford University Press, 2010).
3. Nowak, W. in *Handbook of Computational Chemistry* (ed Leszczynski, J.) 1–43 (Springer Netherlands, Dordrecht, 2016).
4. Goodfellow, I., Bengio, Y. & Courville, A. *Deep Learning* `http://www.deeplearningbook.org` (MIT Press, 2016).
5. Nielsen, M. *Neural networks and machine learning* `http://neuralnetworksanddeeplearning.com/about.html` (2022).
6. Behler, J. Neural network potential-energy surfaces in chemistry: A tool for large-scale simulations. *Physical Chemistry Chemical Physics* **13,** 17930–17955 (2011).
7. Kingma, D. P. & Ba, J. *Adam: A Method for Stochastic Optimization* Jan. 29, 2017. arXiv: `1412.6980[cs]`. (2023).
8. Singraber, A., Morawietz, T., Behler, J. & Dellago, C. Parallel Multistream Training of High-Dimensional Neural Network Potentials. *Journal of Chemical Theory and Computation* **15,** 3075–3092 (2019).
9. Unke, O. T. *et al.* Machine Learning Force Fields. *Chemical Reviews* **121.** ISSN: 0009-2665, 1520-6890. `https://pubs.acs.org/doi/10.1021/acs.chemrev.0c01111` (2023) (Aug. 25, 2021).
10. Behler, J. & Parrinello, M. Generalized neural-network representation of high-dimensional potential-energy surfaces. *Physical Review Letters* **98,** 1–4 (2007).
11. Behler, J. Atom-centered symmetry functions for constructing high-dimensional neural network potentials. *Journal of Chemical Physics* **134** (2011).
12. Pukrittayakamee, A. *et al.* Simultaneous fitting of a potential-energy surface and its corresponding force fields using feedforward neural networks. *J Chem Phys* **130,** 134101 (Apr. 7, 2009).
13. Chowdhury, P. & Sehitoglu, H. Deformation physics of shape memory alloys – Fundamentals at atomistic frontier. *Progress in Materials Science* **88,** 49–88. (2023) (July 2017).

14. *Shape memory materials* (eds Ōtsuka, K. & Wayman, C. M.) (Cambridge University Press, Cambridge ; New York, 1998). 284 pp.

15. Bhattacharya, K., Conti, S., Zanzotto, G. & Zimmer, J. Crystal symmetry and the reversibility of martensitic transformations. *Nature* **428,** 55–59 (2004).

16. Pierre Toledano, V. D. *Reconstructive Phase Transitions: In Crystals and Quasicrystals* (World Scientific, 1996).

17. Ericksen, J. L. Weak Martensitic Transformations in Bravab Lattices.

18. Ericksen, J. L. Some phase transitions in crystals. *Archive for Rational Mechanics and Analysis* **73,** 99–124. (2023) (1980).

19. Gao, Y. *et al.* An origin of functional fatigue of shape memory alloys. *Acta Materialia* **126,** 389–400. (2023) (Mar. 2017).

20. Gao, Y. Symmetry and pathway analyses of the twinning modes in Ni–Ti shape memory alloys. *Materialia* **6,** 100320 (2019).

21. Zelazny, M., Richardson, R. & Ackland, G. J. Twinning hierarchy, shape memory, and superelasticity demonstrated by molecular dynamics. *Physical Review B* **84,** 144113. (2023) (Oct. 18, 2011).

22. Ezaz, T., Wang, J., Sehitoglu, H. & Maier, H. Plastic deformation of NiTi shape memory alloys. *Acta Materialia* **61,** 67–78. (2023) (Jan. 2013).

23. Vítek, V. Intrinsic stacking faults in body-centred cubic crystals. *The Philosophical Magazine: A Journal of Theoretical Experimental and Applied Physics* **18,** 773–786 (1968).

24. Nishida, M. *et al.* New deformation twinning mode of B19 martensite in Ti-Ni shape memory alloy. *Scripta Materialia* **39,** 1749–1754 (1998).

25. Huang, X., Ackland, G. J. & Rabe, K. M. Crystal structures and shape-memory behaviour of NiTi. *Nature Materials* **2,** 307–311. (2023) (May 1, 2003).

26. *VASP* `https://www.vasp.at/` (2022).

27. Kresse, G. & Hafner, J. Ab initio molecular dynamics for liquid metals. *Phys. Rev. B* **47,** 558–561 (1 Jan. 1993).

28. Kresse, G. & Furthmüller, J. Efficiency of ab-initio total energy calculations for metals and semiconductors using a plane-wave basis set. *Computational Materials Science* **6,** 15–50 (1996).

29. Behler, J. Constructing high-dimensional neural network potentials: A tutorial review. *International Journal of Quantum Chemistry* **115,** 1032–1050 (2015).

30. Behler, J. First Principles Neural Network Potentials for Reactive Simulations of Large Molecular and Condensed Systems. *Angewandte Chemie International Edition* **56,** 12828–12840. (2023) (Oct. 9, 2017).

31. *Large-scaleAtomic/MolecularMassivelyParallelSimulator (LAMMPS)* `https://lammps.sandia.gov/`.

32. Thompson, A. P. *et al.* LAMMPS - a flexible simulation tool for particle-based materials modeling at the atomic, meso, and continuum scales. *Comp. Phys. Comm.* **271,** 108171 (2022).

33. Singraber, A., Behler, J. & Dellago, C. Library-Based LAMMPS Implementation of High-Dimensional Neural Network Potentials. *Journal of Chemical Theory and Computation* **15,** 1827–1840 (2019).

34. Pun, G. P. P. & Mishin, Y. Optimized interatomic potential for silicon and its application to thermal stability of silicene. *Phys. Rev. B* **95,** 224103 (22 June 2017).

35. Hall, J. J. Electronic Effects in the Elastic Constants of n-Type Silicon. *Phys. Rev.* **161,** 756–761 (3 Sept. 1967).

36. Kong, L. T., Bartels, G., Campañá, C., Denniston, C. & Müser, M. H. Implementation of Green's function molecular dynamics: An extension to LAMMPS. *Computer Physics Communications* **180,** 1004–1010 (2009).

37. Togo, A., Chaput, L., Tadano, T. & Tanaka, I. Implementation strategies in phonopy and phono3py. *J. Phys. Condens. Matter* **35,** 353001 (2023).

38. Togo, A. First-principles Phonon Calculations with Phonopy and Phono3py. *J. Phys. Soc. Jpn.* **92,** 012001 (2023).

39. Zhou, F., Nielson, W., Xia, Y. & Ozolins, V. Lattice anharmonicity and thermal conductivity from compressive sensing of first-principles calculations. *Physical Review Letters* (Apr. 2014).

40. Ko, W.-S., Grabowski, B. & Neugebauer, J. Development and application of a Ni-Ti interatomic potential with high predictive accuracy of the martensitic phase transition. *Phys. Rev. B* **92,** 134107 (13 Oct. 2015).

41. Ren, G. & Sehitoglu, H. Interatomic potential for the NiTi alloy and its application. *Computational Materials Science* **123,** 19–25. (2023) (Oct. 2016).

42. Kudoh, Y., Tokonami, M., Miyazaki, S. & Otsuka, K. Crystal structure of the martensite in Ti-49.2 at.%Ni alloy analyzed by the single crystal X-ray diffraction method. *Acta Metallurgica* **33,** 2049–2056 (1985).

43. Wang, J. & Sehitoglu, H. Martensite modulus dilemma in monoclinic NiTi-theory and experiments. *International Journal of Plasticity* **61,** 17–31 (2014).

44. Wagner, M.-X. & Windl, W. Lattice stability, elastic constants and macroscopic moduli of NiTi martensites from first principles. *Acta Materialia* **56,** 6232–6245 (2008).

45. Wu, Z. & Lawson, J. W. Theoretical investigation of phase transitions in the shape memory alloy NiTi. *Phys. Rev. B* **106,** L140102. (2023) (Oct. 14, 2022).

46. Hirth, J. P., Lothe, J. & Mura, T. Theory of dislocations. *Journal of Applied Mechanics* **50,** 476–477 (1983).